



# Improvement of ferroelectric properties via Zr doping in barium titanate nanoparticles

Mahasen Reda<sup>1</sup>, S. I. El-Dek<sup>2</sup>, and M. M. Arman<sup>1,\*</sup>

<sup>1</sup> Materials Science Laboratory (1), Physics Department, Faculty of Science, Cairo University, Giza, Egypt

<sup>2</sup> Materials Science and Nanotechnology Department, Faculty of Postgraduate Studies for Advanced Sciences (PSAS), Beni-Suef University, Beni-Suef, Egypt

Received: 2 February 2022

Accepted: 7 June 2022

Published online:

26 June 2022

© The Author(s) 2022

## ABSTRACT

Barium titanate is still the prototype of a piezoelectric crystalline material that has attracted many researchers and industrial partners to use. A modified citrate method was used to create barium titanate nanoparticles  $\text{BaTi}_{1-x}\text{Zr}_x\text{O}_3$ . The samples were crystallized in a single-phase tetragonal structure, as revealed using X-ray powder diffraction. The crystallite size decreases with increasing Zr concentration. Fourier-transform infrared spectra showed the main absorption bands of the samples  $\text{BaTi}_{1-x}\text{Zr}_x\text{O}_3$ . Field emission scanning electron microscopy micrographs illustrate that the doped sample  $\text{BaTi}_{0.9}\text{Zr}_{0.1}\text{O}_3$  is more porous and finer than the parent. For low Zr doping concentrations ( $x = 0.1$ ), the ferroelectric properties of barium titanate are improved. The conduction mechanisms in the samples are small polaron hopping and correlated barrier hopping. The Zr/Ti ratio is a crucial parameter for tailoring the ferroelectric–paraelectric phase transition.

## 1 Introduction

Barium titanate ( $\text{BaTiO}_3$ ) with a tetragonal perovskite structure has many features, such as high dielectric permittivity at room temperature, ferroelectricity, and low leakage current [1].  $\text{BaTiO}_3$  is a ferroelectric material that belongs to the family of  $\text{ABO}_3$  perovskite structures, where 'A' is the site of  $\text{Ba}^{2+}$  and 'B' is the site of  $\text{Ti}^{4+}$ , which are the two cations of the perovskite structure which are of different sizes, and O is the oxygen anion that bonds to both cations [2, 3]. The smaller cation, which occupies the B site of the perovskite structure with the largest charge, must be a transition metal, like  $\text{Ti}^{4+}$  ion with a radius of about

(0.605 Å), or  $\text{Zr}^{4+}$  ion with a radius of about (0.72 Å) [3, 4]. The biggest cation, which occupies the A site of the perovskite structure like  $\text{Ba}^{2+}$  ion with a radius of about (1.61 Å) is with a charge smaller than the B cation, where both the sum of charge positive ions A and B together is equal to 6. The B cation is octahedrally coordinated by the oxygen anions  $\text{O}^{2-}$  [4].

$\text{BaTiO}_3$  has polymorphic phase transitions according to different temperature ranges, rhombohedral (below  $-90^\circ\text{C}$ ), by increasing temperature it converts from rhombohedral to orthorhombic phase at about  $-90^\circ\text{C}$  and then it converts to tetragonal at about  $5^\circ\text{C}$  and then to cubic phase at about  $120^\circ\text{C}$  [2, 5].

Address correspondence to E-mail: mmarmsci@gmail.com

BaTiO<sub>3</sub> was thought to be a promising material for a variety of applications, including dynamic random access memory (DRAM) processing, other integrated condenser structures, electronic device manufacturing, and high-frequency filters [6, 7]. Barium titanate perovskite was preferred for use in ceramic capacitors owing to their high energy density values [8, 9]. However, pure BaTiO<sub>3</sub> has a hysteresis phenomenon and losses associated with it, which ultimately lead to significantly reduced energy density values [10]. According to the shape of the P–E loop and the dependence of dielectric permittivity on frequency, the ferroelectric materials can be classified into relaxor or classical ferroelectrics. Relaxor ferroelectrics are characterized by a broad and frequency-dependent maximum of the dielectric permittivity as a function of temperature. While classical ferroelectrics have a sharp and frequency-independent dielectric permittivity. The properties of relaxors generally originate due to the presence of randomly orientated polar nanoregions [11, 12]

Many researchers have been interested in studying the different properties of barium titanate. Roussin Lontio Fomekong reported that Rh<sup>3+</sup>-doped BaTiO<sub>3</sub> has been prepared by the oxalate coprecipitation route for applications such as exhaust emission control [13], Wei Li prepared Zr-doped BaTiO<sub>3</sub> using a solid-state reaction technique and reported that BaTi<sub>0.85</sub>Zr<sub>0.15</sub>O<sub>3</sub> has the highest dielectric constant obtained, which is about 15,900 [14], and Ning Wang prepared co-doped barium titanate with the formula Ba(Ti<sub>0.94</sub>Sn<sub>0.06–x</sub>Zr<sub>x</sub>)O<sub>3</sub> (0.00 ≤ *x* ≤ 0.06) and reported that the highest *P<sub>r</sub>* = 9.5 μC/mm<sup>2</sup>, the lowest *E<sub>c</sub>* = 2.5 kV/cm and the highest relative dielectric constant *ε<sub>r</sub>* = 7513 at the Curie temperature *T<sub>c</sub>* all were obtained at *x* = 0.00 but *T<sub>c</sub>* moves towards higher temperatures by increasing Zr content [15]. By the modified citrate auto-ignition method, M.A. Ahmed succeeded in synthesizing BaTiO<sub>3</sub> with crystallite size of around 47 nm with a rod shape [16]. T. K. KUNDU synthesized nickel (Ni) and iron (Fe) ion doped BaTiO<sub>3</sub> nanoparticles using chemical route method by a general formula, Ba(Ti<sub>1–z</sub>X<sub>z</sub>)O<sub>3</sub>, where [X: Fe and Ni] with *z* = 0.03, 0.06, 0.1, 0.16, and 0.2 with an average grain sizes lies between 24 and 49 nm [17]. The authors reported that the dielectric permittivity is enhanced in doped samples by an order of magnitude compared to the parent, and it shows maxima at *z* = 0.03 for Fe-doped BaTiO<sub>3</sub> and *z* = 0.06 for Ni-doped BaTiO<sub>3</sub> [17]. Das employed a

solid-state sintering technique for synthesizing Ni-doped barium titanate of BaTi<sub>1–x</sub>Ni<sub>x</sub>O<sub>3</sub> (here, *x* = 0, 0.05, 0.1, and 0.15). The author mentioned that by increasing doping with Ni, magnetism is induced and it is also enhanced. Saturation electric polarization values and the shape of ferroelectric hysteresis loops of doped compositions experience a big change with increasing Ni content [18].

Since lead zirconate titanate (PZT) is one of the important ferroelectric materials (typical ferroelectric material), we aimed to prepare a free lead ferroelectric material. Therefore, we think about using zirconium and titanium together with barium. We want to prepare a (BZT) ceramic material that competes with (PZT) in ferroelectrical properties without lead. We take Barium Titanate nanoparticles in the range BaTi<sub>1–x</sub>Zr<sub>x</sub>O<sub>3</sub> (BTZ) (0 ≤ *x* ≤ 0.3) as a starting attempt to check how much Zr concentrations maintain the stability of the structure. In the future, we will investigate the effect of rich doping Zr-(BTZ) as well as the effect of a new dopant in addition to co-doping ceramics.

Whereas the preparation of a higher concentration of Zr-doped BaTiO<sub>3</sub> is not common, we were able to prepare a single-phase tetragonal nanostructure at a higher concentration (*x* = 0.3) using cheaper raw materials and easier and faster methods than other reported literature at lower annealing times and temperatures, which reduces the overall cost.

We have been keen to study many of the physical properties of Zr-doped BaTiO<sub>3</sub> in this paper. We have made a comparison between our samples and the literature. This study of Zr-doped BaTiO<sub>3</sub> serves as a starting point. Our future work is to make co-doped BaTiO<sub>3</sub> and insert them into polymers and try to fabricate nanofibers. Therefore, we had to study the effect of higher zirconium concentration. Our aim in this work is to examine the effect of higher Zr substitution on the Ti site to find how much the structure will remain stable without any distortion. The structure and morphology of the sample were studied using XRD, FTIR, and FESEM. In this piece of work, the improvement of the physical and dielectric ferroelectric properties of BaTiO<sub>3</sub> nanoparticles by Zr substitution at the expense of titanium ions was examined. The properties of BaTiO<sub>3</sub> can be tuned by the Zr concentration of doping. The dielectric and ferroelectric properties of Zr-doped barium titanate nanoparticles are examined and correlated together with morphology and microstructure and discussed.

## 2 Experimental techniques

### 2.1 Preparation of pure barium titanate and Zr-doped barium titanate nanoparticles

#### 2.1.1 Preparation of barium titanate ( $\text{BaTiO}_3$ ) nanoparticles

Figure 1 indicates the flowchart that was followed for preparing the Zr-doped Barium Titanate ( $\text{BaTi}_{1-x}\text{Zr}_x\text{O}_3$ ;  $x = 0.0, 0.1, 0.2,$  and  $0.3$ ) nanoparticles using the modified citrate method [19]. As starting materials, the precursors Barium Nitrate [ $\text{Ba}(\text{NO}_3)_2$ , 99.9%] (Sigma-Aldrich), tetrabutyl titanate [ $\text{Ti}(\text{OC}_4\text{H}_9)_4$ , 97%), and citric acid were used.

In separate beakers, 1 mol of  $\text{Ba}(\text{NO}_3)_2$  and 2 mol of citric acid were dissolved in sufficient deionized water to make complete solutions, and 1 mol of tetrabutyl titanate was suspended in sufficient deionized water and mixed well with the citric acid solutions on the magnetic stirrer at  $70^\circ\text{C}$  for 1 h. Then a barium nitrate solution was added. Then the power of hydrogen (pH) was adjusted to 8.

The temperature of the mixture was raised to  $120^\circ\text{C}$  with continuous stirring until all the volatile components and water from the beaker evaporated.

After that, the mixture appeared to be slightly thick and sticky and was then left to burn completely on the hot plate to obtain black fine powder. The black powder was annealed at  $1100^\circ\text{C}$  for 2 h with a heating rate of  $5^\circ\text{C}/\text{min}$  in a furnace. A white fine powder was formed after the annealing process in which the  $\text{BaTiO}_3$  was formed.

#### 2.1.2 Preparation of Zr-doped barium titanate ( $\text{BaTi}_{1-x}\text{Zr}_x\text{O}_3$ ) nanoparticles

To make Zr-doped Barium Titanate, the same steps are followed, except that ( $x$ ) mol of Zirconium Oxychloride [ $\text{ZrOCl}_2$ , 99.9%] (Sigma-Aldrich), solution is added to a  $(1 - x)$  mol of butyl titanite suspension with the appropriate concentrations according to the formula:  $\text{BaTi}_{1-x}\text{Zr}_x\text{O}_3$ .

### 2.2 Characterization and measurements of the obtained samples

X-ray powder diffraction (XRD) was used in the investigation of the crystallinity of the samples using a Bruker advanced D8 X-ray diffractometer. The pattern was recorded using  $\text{Cu-K}_\alpha$  radiation ( $\lambda_D = 1.54182 \text{ \AA}$ ) in the  $2\theta$  range  $20\text{--}80^\circ$ . XRD pattern was indexed according to the International Centre for

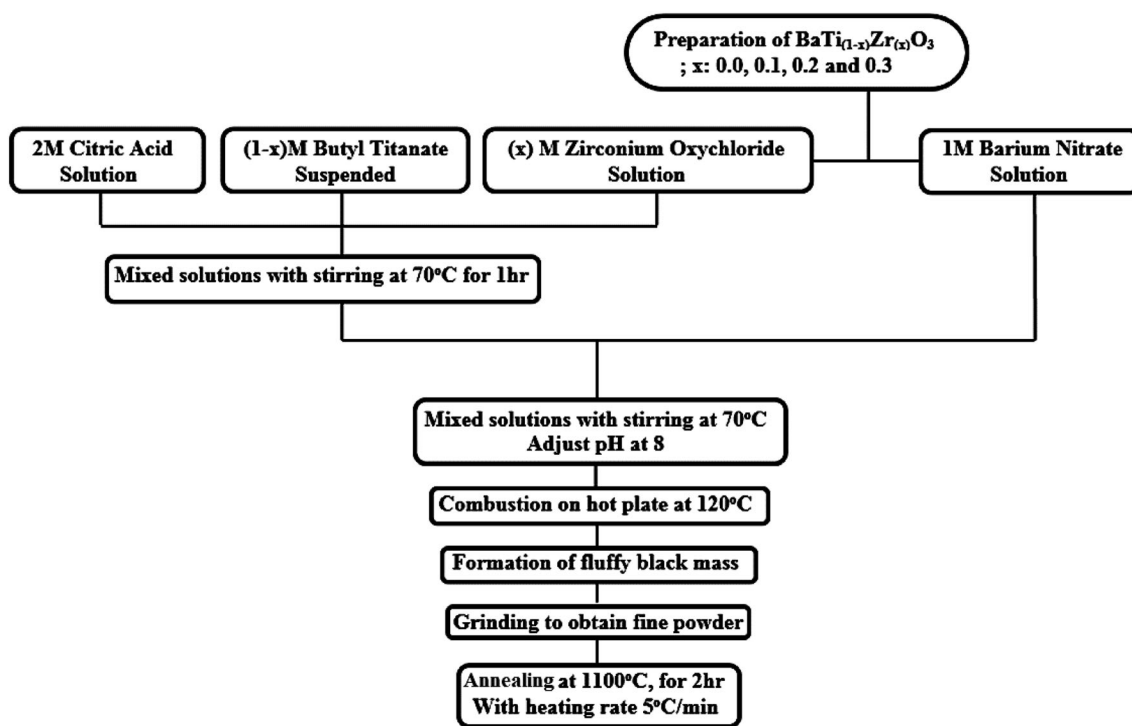


**Fig. 1** Flowchart of the preparation of the  $\text{BaTi}_{(1-x)}\text{Zr}_{(x)}\text{O}_3$ ; ( $x = 0.0, 0.1, 0.2,$  and  $0.3$ )

Diffraction Data (ICDD) card number 04-016-2039. Fourier Transform Infrared spectra (FT-IR) were recorded for all using a VERTEX 70 FT-IR spectrophotometer (Bruker Optics, Germany). The samples were prepared for FTIR measurements by mixing 95% of the KBr with 5% of the sample and grinding them well. A manual piston has been used to pelletize the sample in the form of a transparent disc. The surface morphology of sintered samples was imaged using field emission scanning electron microscopy (FESEM) Model Quanta 250 FEG (Field Emission Gun) attached with an EDAX unit (energy-dispersive X-ray analysis). For the dielectric, ferroelectric and DC conductivity measurements, we pressed the prepared powders using a uniaxial press of value  $8 \times 10^5 \text{ N/m}^2$  into 10 mm-diameter pellets with a thickness of 4.58, 4.02, 4.02, and 3.91 mm for  $x = 0.0, 0.1, 0.2,$  and  $0.3$  respectively. Then it was annealed at  $500 \text{ }^\circ\text{C}$  for 1 h. with a heating rate of  $5 \text{ }^\circ\text{C/min}$  in a muffle furnace to obtain a denser ceramic. Electrodes were made using silver paste on both surfaces of the pellet and then checked for good conduction. Dielectric measurements were performed using an LCR meter (Hioki model 3532 Japan) at different frequencies and temperatures. DC conductivity and  $I$ - $V$  characteristic data were measured in the temperature range of  $300$ – $800 \text{ K}$  by using a Picoammeter Keithley 485. The polarization  $P$  was measured as a function of the electric field  $E$  at room temperature using a homemade Sawyer–Tower circuit. OriginPro 8 software was used to create the artwork.

### 3 Results and discussion

#### 3.1 XRD analysis

Figure 2a shows the XRD patterns of the samples with the general formula  $\text{BaTi}_{1-x}\text{Zr}_x\text{O}_3$ ; ( $x: 0.0, 0.1, 0.2,$  and  $0.3$ ). The investigated samples were crystallized in a single-phase possessing the tetragonal space group  $P4\text{mm}$  with one molecule per unit cell. The lattice parameters were calculated and indexed with all the peaks in the XRD patterns compared with the ICDD card number (04-016-2039). Table 1 shows the values of the lattice parameter ( $a_{\text{exp}}$  and  $c_{\text{exp}}$ ), the crucial ratio ( $c/a$ ), the unit cell volume, the position of the most intense peak ( $2\theta$ ), the crystallite size ( $L$ ), the theoretical density ( $D$ ), the tolerance factor ( $t$ ), and

the average grain size for the samples  $\text{BaTi}_{1-x}\text{Zr}_x\text{O}_3$ ; ( $x: 0.0, 0.1, 0.2,$  and  $0.3$ ).

The lattice parameter was calculated from Eq. (1):

$$\frac{1}{d^2} = \frac{h^2 + k^2}{a^2} + \frac{l^2}{c^2} \quad (1)$$

where  $h, k,$  and  $l$  are the Miller indices detected from the ICDD card, and  $d$  is the interplanar spacing based on tetragonal symmetry.

Both lattice parameters ( $a, c$ ) for  $\text{BaTi}_{1-x}\text{Zr}_x\text{O}_3$  powders increased when doping the tetragonal lattice due to the substitution of  $\text{Ti}^{4+}$  (radii =  $0.605 \text{ \AA}$ ) by the larger  $\text{Zr}^{4+}$  ion (radii =  $0.72 \text{ \AA}$ ). Also, the electron cloud density of a Zr atom with an electronic configuration of  $[\text{Kr}] 4d^2 5s^2$  and the electronic configuration of the  $\text{Zr}^{4+}$  ion ( $1s^2 2s^2 2p^6 3s^2 3p^6 3d^{10} 4s^2 4p^6$ ) causes its atomic and ionic size to be larger than that of a Ti atom and  $\text{Ti}^{4+}$  ion with an electronic configuration of  $[\text{Ar}] 4s^2 3d^2$  and ( $1s^2 2s^2 2p^6 3s^2 3p^6$ ), respectively. It leads to an increase in the interplanar spacing of the crystal, which in turn increases the lattice parameters.

Because the electronic density and ionic radii of  $\text{Zr}^{4+}$  (radius of  $0.72 \text{ \AA}$ ) and  $\text{Ti}^{4+}$  (radius of  $0.605 \text{ \AA}$ ) differ, the lattice parameters ( $a, c$ ) of the samples increase as Zr content increases, resulting in an increase in unit cell volume [20].

There is a relation between the interplanar spacing of the crystal ( $d$ ) and the angle of incidence ( $\theta$ ) known as Bragg's Law, which is expressed by the Eq. (2) [21]:

$$n\lambda = 2d \sin \theta \quad (2)$$

where  $n$  (an integer) is the "order" of reflection ( $n = 1$ ), and  $\lambda$  is the wavelength of the incident X-rays.

From Eqs. (1) and (2), we can obtain  $\theta$  for the most intense peak (101) as a function of the lattice parameters by the following expression in Eq. (3):

$$\theta = \sin^{-1} \left( \frac{\lambda \sqrt{a^2 + c^2}}{2ac} \right) \quad (3)$$

Therefore, with the increase in Zr content, the lattice parameters increase, and thus the angle  $\theta$  decreases; therefore, we obtained a shift in the most intense peak towards lower  $2\theta$ . It was calculated for each sample, and the calculated values were listed in Table 1 for clarification. This shift to lower values is illustrated also in Fig. 2b due to the increase in the

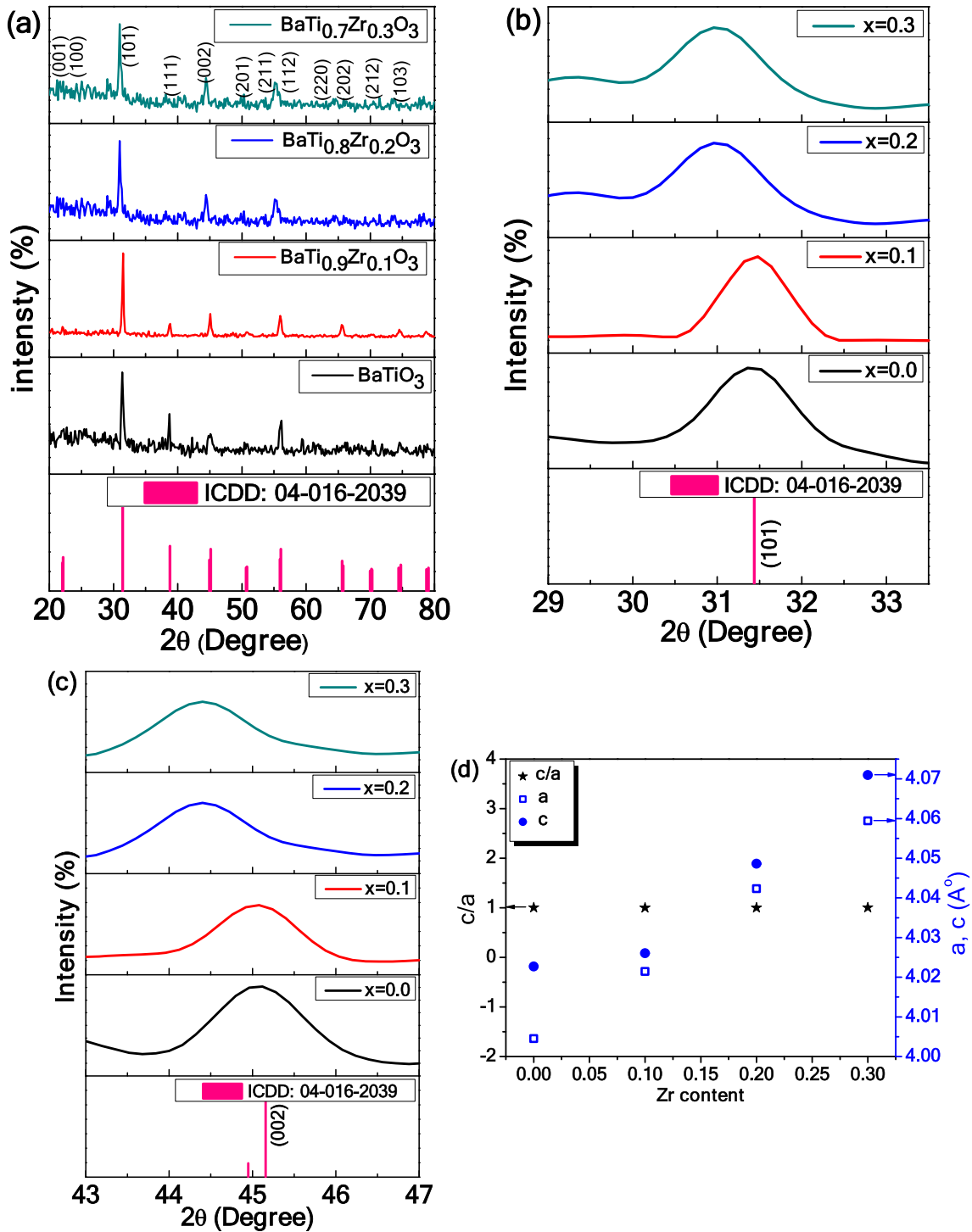


**Fig. 2** a XRD pattern of nanopowder  $\text{BaTi}_{1-x}\text{Zr}_x\text{O}_3$ ; ( $x$ : 0.0, 0.1, 0.2, and 0.3). b magnified pattern of (101) peaks. c Magnified pattern of (002) peaks illustrating the shift of the patterns. d Dependence of lattice parameter on Zr content

unit cell parameter, which agrees with the report of Deluca et al. [22]. The tendency of the peak (002) to decrease as the zirconium content increased was interpreted as owing to the larger radius of  $\text{Zr}^{4+}$  than

$\text{Ti}^{4+}$ . This enhances the tetragonality as shown in Fig. 2c [22, 23].

From a closer look at Fig. 2d, the lattice parameter ( $a$ ) was increased linearly with  $\text{Zr}^{4+}$  content, obeying

**Table 1** Values of the lattice parameter ( $a_{\text{exp}}$  and  $c_{\text{exp}}$ ), the crucial ratio ( $c/a$ ) the unit cell volume, the position of the most intense peak ( $2\theta$ ), the crystallite size ( $L$ ), the theoretical density ( $D_x$ ) and the tolerance factor for the samples  $\text{BaTi}_{1-x}\text{Zr}_x\text{O}_3$  ( $x = 0, 0.1, 0.2$  and  $0.3$ )

	$a_{\text{exp}}$ (Å)	$c_{\text{exp}}$ (Å)	$c/a$	$2\theta$	Volume (Å <sup>3</sup> )	$L$ (nm)	$D_x$ (gm/cm <sup>3</sup> )	$t$	Grain size (nm)
$\text{BaTiO}_3$	4.005	4.023	1.0045	31.5201	64.51	38	6.002	1.071	355
$\text{BaTi}_{0.9}\text{Zr}_{0.1}\text{O}_3$	4.021	4.026	1.0011	31.4435	65.11	23	6.057	1.064	130
$\text{BaTi}_{0.8}\text{Zr}_{0.2}\text{O}_3$	4.042	4.049	1.0016	31.2682	66.12	19	6.070	1.058	145
$\text{BaTi}_{0.7}\text{Zr}_{0.3}\text{O}_3$	4.059	4.071	1.0029	31.1144	67.08	19	6.093	1.052	214

Vegard's law. The ( $c$ ) parameter increased also, but with a different trend. The crucial ratio that could better describe the tetragonal symmetry is  $c/a$ . Hence, in our situation, the  $c/a$  ratio is always greater than unity, which simply means the elongation of the  $\langle \text{TiO}_6 \rangle$  octahedron along the  $Z$ -axis, keeping the symmetry unchanged. This is an indication of the proper choice of  $\text{Zr}^{4+}$  as a dopant and the range of concentration as well.

The average crystallite size was calculated from the well-known Scherrer's Eq. (4) [24–26]:

$$L = \frac{K\lambda}{\beta \cos \theta} \quad (4)$$

where  $L$  is the average crystallite size,  $\lambda$  is the X-ray wavelength,  $\theta$  is the Bragg angle,  $\beta$  is the corrected full width at half maximum (FWHM) of the X-ray peak on the  $2\theta$  axis, and  $K$  is the so-called Scherrer constant.  $K$  depends on the crystallite shape and the size distribution, indices of the diffraction line, and the actual definition used for  $\beta$  whether FWHM or integral breadth [27].  $K$  can have values anywhere from 0.62 to 2.08. In this paper,  $K = 0.9$  was used. The samples exhibited a low crystallite size (between 19 and 38 nm). The background in XRD patterns could be originated from small crystallite size of the samples prepared.

The unit cell volume was calculated from  $V = a^2 \times c$ , and the values listed in Table 1. The tetragonal matrix of  $\text{BaTiO}_3$  was found to increase significantly by doping with zirconium as it got enlarged from 64.51 Å at ( $x = 0$ ) to 67.1 Å at ( $x = 0.3$ ) by an increase of 4% with an increase of 30% zirconium.

The theoretical density ( $D_x$ ) was calculated from the Eq. (5) [28, 29]

$$D_x = \frac{ZM}{N_A V} \quad (5)$$

where  $Z$  is the number of molecules per unit cell,  $N_A$  is the Avogadro's number,  $V$  is the unit cell volume,

and  $M$  is the molecular weight of  $\text{BaTi}_{1-x}\text{Zr}_x\text{O}_3$ , which is calculated from the Eq. (6):

$$M = m_{\text{Ba}} + (1 - x) \times m_{\text{Ti}} + (x) \times m_{\text{Zr}} + 3 \times m_{\text{O}} \quad (6)$$

where  $m_{\text{Ba}}$  is the atomic weight of the barium atom,  $m_{\text{Ti}}$  is the atomic weight of the titanium atom,  $m_{\text{Zr}}$  is the atomic weight of the zirconium atom, and  $m_{\text{O}}$  is the atomic weight of the oxygen atom. The density increased by 0.25% despite the increase in volume because the molecular weight of doped  $\text{BaTi}_{1-x}\text{Zr}_x\text{O}_3$  samples increased by a greater percentage than the volume augmentation as the zirconium concentration increased.

The difference in molecular weight compensated for the increase in volume. That is because the overall values of the densities are getting greater. This is a benefit as the materials become denser and this contributes to reducing the porosity causing the current leakage.

The tolerance factor is a common geometrical factor that indicates the stability of the perovskite structure. This factor gives a good prediction of how far the A site cation is suitable within the cavities in the  $\langle \text{BO}_6 \rangle$  [30]. A tolerance factor of 1 indicates an ideal fit [30]. However for  $0.77 < t < 1.10$ , the perovskite structure remains stable also [31]. But for  $t < 0.77$ , this indicates that the A cation is too small, which leads to a reduction in the symmetry due to the tilting of the  $\text{BO}_6$  octahedra, leading to an increase in distortion. If  $t > 1.1$ , this indicates that the A site cation is too large and a perovskite structure is not formed [30].

The tolerance factor of the investigated samples was calculated according to the general formula (7):

$$t = \frac{r_A + r_O}{\sqrt{2}(r_B + r_O)} \quad (7)$$

where,  $r_A$ ,  $r_B$ , and  $r_O$  are the ionic radii of the A, B, and oxygen ions, respectively [32, 33].

The values of the tolerance factor were reported in Table 1 and indicate the formation of the investigated samples in a tetragonal phase, which agrees with the data obtained from XRD. The tolerance factor decreases with increasing the Zr content on the B site due to increasing the effective B ionic radius  $r_B$  where the ionic radius of the  $Zr^{4+}$  ion is 0.72 Å and that of the  $Ti^{4+}$  ion is 0.605 Å [24]. According to Eq. (5), by increasing the ionic radius  $r_B$  the tolerance factor decreases, which means that the distortion in the perovskite structure also increases.

### 3.2 FESEM images analysis

The morphology of perovskite strongly depends on the type and concentration of the doping metal ions. Figure 3a shows the field emission scanning electron microscope of the samples  $BaTi_{1-x}Zr_xO_3$ . FESEM images are required to study the surface morphology of the investigated powder. The images illustrate the agglomeration of grains of various sizes. The average grain size of each sample range is reported in Table 1. A representative histogram of the grain size distribution of the samples is shown in Fig. 3b. The average grain size decreased by adding  $Zr^{4+}$  ion. We obtained the smallest average grain size at ( $x = 0.1$ ), where it is reduced to 36.6% of the parent one. By adding more zirconium, the grain size begins to increase and is comparable to the sample at ( $x = 0.1$ ), but it becomes 41% of the parent sample at ( $x = 0.2$ ) and 60.2% of the parent sample at ( $x = 0.3$ ). From the FESEM images, we observe the presence of an intragranular porosity of the parent sample  $BaTiO_3$  and the doped one at ( $x = 0.1$ ) more than the other Zr-doped samples. As a result, the samples could be tested in a variety of applications, including heavy metal and dye removal. The doping with  $Zr^{4+}$  ion in the sample  $BaTiO_3$  at the expense of  $Ti^{4+}$  could also lead to a decrease in the crystal size [34]. Figure 4 shows the EDAX of the sample  $BaTi_{0.9}Zr_{0.1}O_3$ . The values of weight and atomic percentages of the different elements are reported in Table 2. The small variation in weight percentage (wt%) between the theoretical calculation and experimental data of oxygen ions from EDS could be the result of annealing the samples at a relatively high temperature as well as some oxygen deficiency.

### 3.3 FTIR analysis

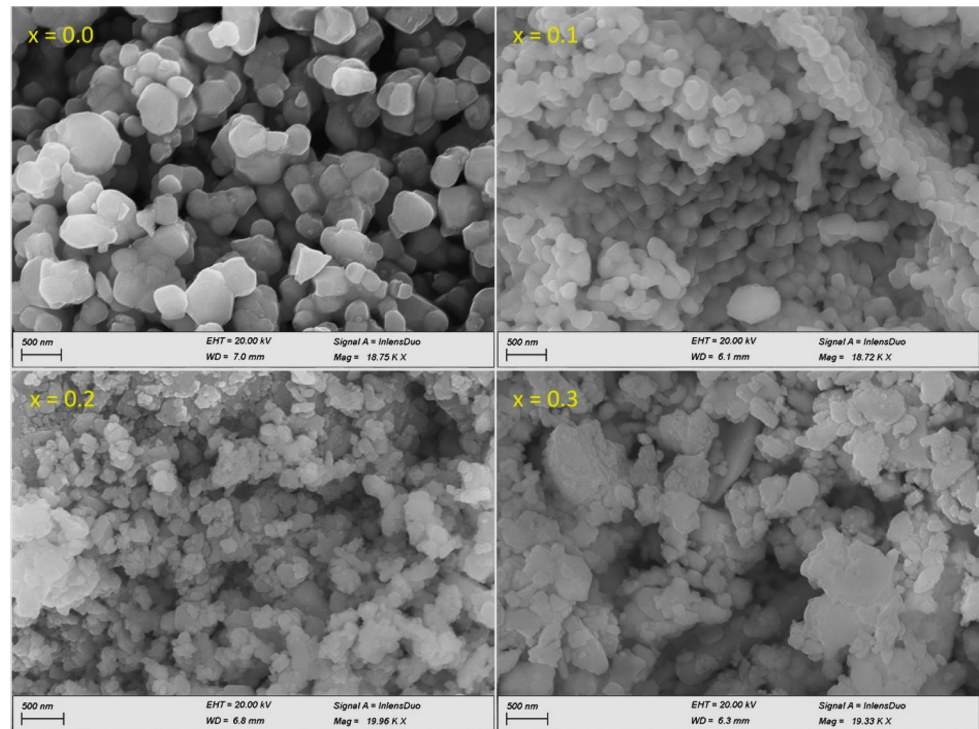
Figure 5 shows the FTIR spectra of the investigated samples  $BaTi_{1-x}Zr_xO_3$ ; ( $x$ : 0.0, 0.1, 0.2, and 0.3). The chart shows the main absorption bands of the investigated samples  $BaTi_{1-x}Zr_xO_3$ . Table 3 shows the values of the FTIR bands of the investigated samples. The Ti–O–Ti and Zr–O–Zr stretching vibrations appear in the  $544\text{--}573\text{ cm}^{-1}$  range, depending on the Zr concentration, which can be attributed to the band's broadness [35–37]. The change that appeared to the Ti–O bond indicates that the  $Ti^{4+}$  ions on the B site of the perovskite structure  $ABO_3$  are well substituted by the  $Zr^{4+}$  ion as mentioned in the XRD patterns. In fact, by magnifying the image and zooming in on it, we found that there is a shift towards the higher wavenumber by adding zirconium, and then by adding more zirconium at ( $x = 0.3$ ), this shift returns to be in the lower wavenumber. This means that there is a change in bond length and bond angle. By calculating the tolerance factor, it was found that it decreased by adding more zirconium. This means that the more zirconium, the greater the distortion. This distortion can be in the form of a tilting in the  $\langle TiO_6 \rangle$  octahedron, and this tilting has an angle. To know at which concentration this tilting is effective, we must calculate the angle of this tilting for each zirconium concentration from the XRD refinement, which will be the focus of our future work. The two bands at around  $1400$  and  $1600\text{ cm}^{-1}$  are also considered as intrinsic signals belonging to  $BaTiO_3$  [38]. The band at  $2360\text{ cm}^{-1}$  indicates the presence of an OH group [39]. The broad bands in the range of  $3200\text{--}3500\text{ cm}^{-1}$  have been attributed to stretching vibrations of OH groups due to surface adsorbed water molecules [4, 19].

### 3.4 Ferroelectric characterization

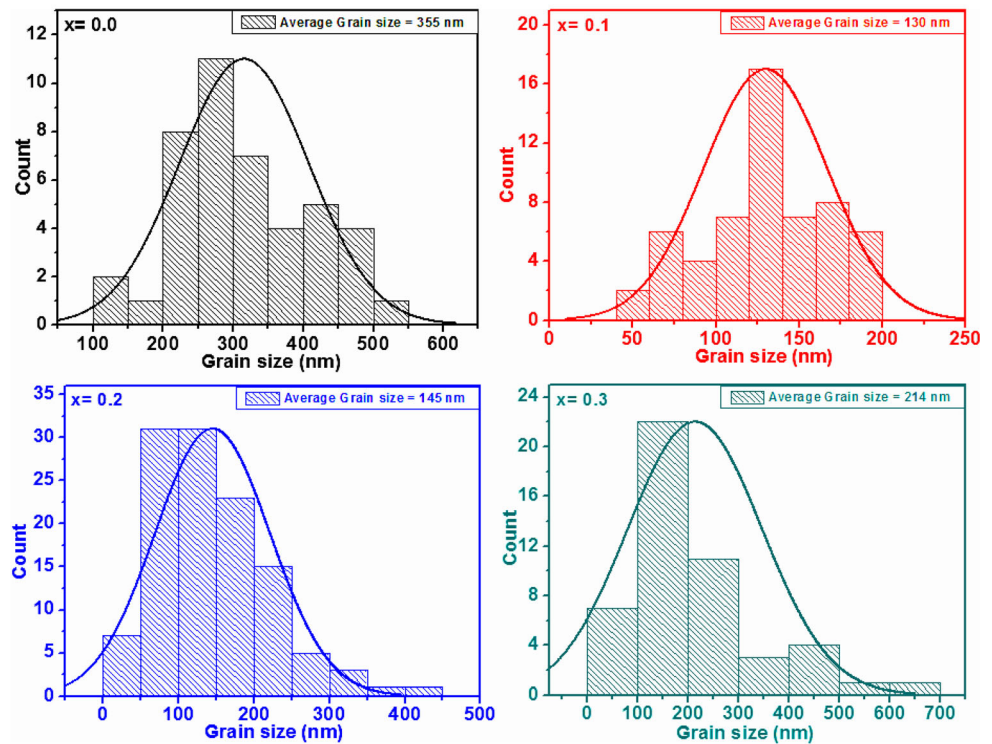
#### 3.4.1 (P–E) hysteresis loops analysis

Figure 6a–d illustrates the P–E hysteresis loop for the investigated samples at room temperature. The P–E hysteresis loops ensure that the samples have ferroelectric behaviour due to the lack of a centre of symmetry in the tetragonal crystal. The values of

**Fig. 3** **a** FESEM of the samples  $\text{BaTi}_{(1-x)}\text{Zr}_x\text{O}_3$ ; ( $x$ : 0.0, 0.1, 0.2, and 0.3). **b** The histogram of grain size distribution where the solid line represents the normal distribution fit of the samples  $\text{BaTi}_{(1-x)}\text{Zr}_x\text{O}_3$ ; ( $x$ : 0.0, 0.1, 0.2, and 0.3)



(a)



(b)

saturation polarization ( $P_s$ ), the remnant polarization ( $P_r$ ), the coercive field ( $E_c$ ), and the breakdown strength (BDS) are reported in Table 4.

It is observed that the ferroelectric properties of barium titanate are improved by low doping ( $x = 0.1$ ). For the  $\text{BaTiO}_3$ , the P–E loop seems to be



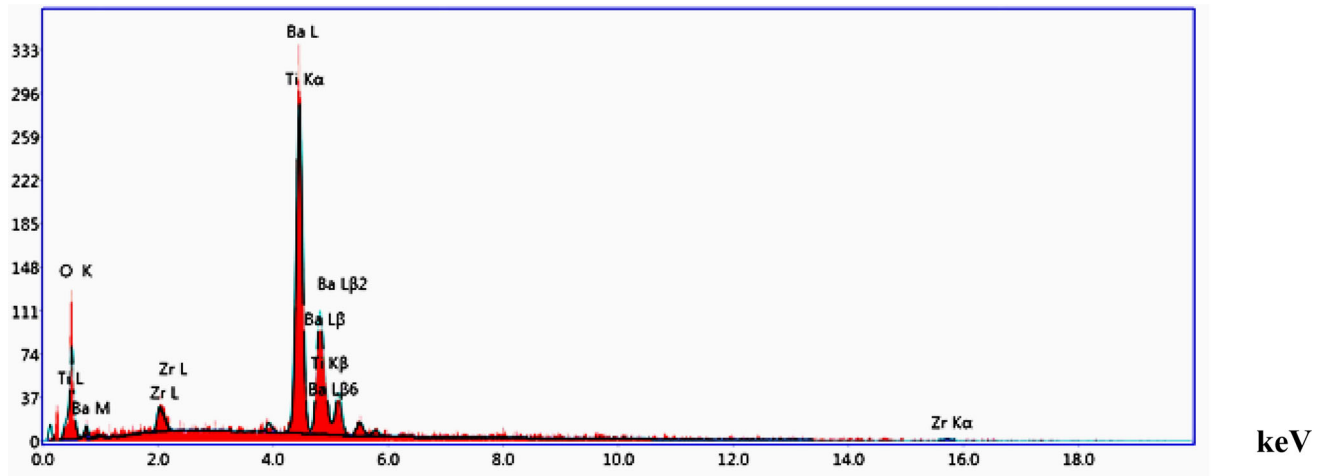


Fig. 4 EDAX of the sample BaTi<sub>0.90</sub>Zr<sub>0.10</sub>O<sub>3</sub>

Table 2 EDX of the sample BaTi<sub>0.90</sub>Zr<sub>0.10</sub>O<sub>3</sub>

Element	Weight % EDX analysis	Weight % Theoretical	Atomic % EDX analysis	Atomic % theoretical
O K	13.05	20.20	50.17	60
Zr L	3.12	3.84	2.11	2
Ba L	71.65	57.82	32.09	20
Ti K	12.17	18.14	15.63	18

Table 3 Values of FTIR bands for the samples BaTi<sub>1-x</sub>Zr<sub>x</sub>O<sub>3</sub> (x = 0, 0.1, 0.2 and 0.3)

	γ <sub>1</sub> (cm <sup>-1</sup> )	γ <sub>2</sub> (cm <sup>-1</sup> )	γ <sub>3</sub> (cm <sup>-1</sup> )	γ <sub>4</sub> (cm <sup>-1</sup> )	γ <sub>5</sub> (cm <sup>-1</sup> )
BaTiO <sub>3</sub>	557	1443	1653	2378	3426
BaTi <sub>0.9</sub> Zr <sub>0.1</sub> O <sub>3</sub>	561	1450	1628	2378	3435
BaTi <sub>0.8</sub> Zr <sub>0.2</sub> O <sub>3</sub>	573	1417	1623	2379	3320–3440
BaTi <sub>0.7</sub> Zr <sub>0.3</sub> O <sub>3</sub>	544	1417	1619	2379	3319–3446

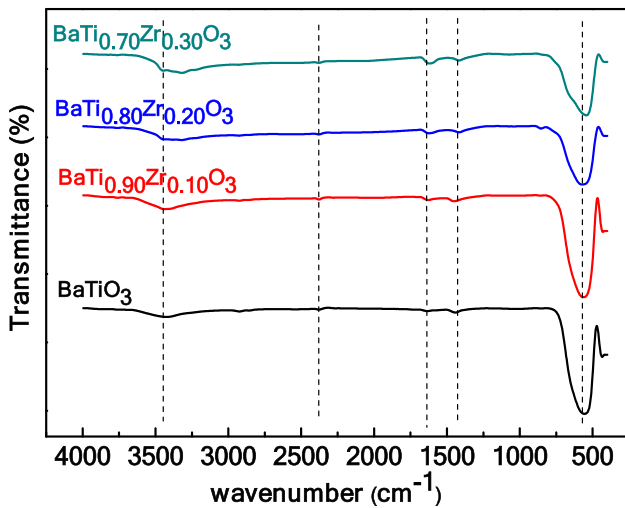


Fig. 5 FTIR of the samples BaTi<sub>(1-x)</sub>Zr<sub>(x)</sub>O<sub>3</sub>; (x: 0.0, 0.1, 0.2, and 0.3)

thin and unsaturated with large polarization values and a very small area of  $= 7.45 \times 10^{-4}$  (J/cm<sup>3</sup>), pointing to a small coercive field value. By doping the BaTiO<sub>3</sub> lattice with Zr, the P–E loop gets larger, the area of the hysteresis loop increases by about 5.5

times from the parent sample,  $E_c$  increases by about 3.5 times and becomes more saturated, but it seems to be completely saturated at higher electric field values than the range of measurements. Increasing the Zr content up to (x = 0.2) increases the coercive field and the loop area by about 2.5 and 2.2 times more than that of the parent sample, respectively. The P–E loops observed in the BaTiO<sub>3</sub>, BaTi<sub>0.9</sub>Zr<sub>0.1</sub>O<sub>3</sub>, and BaTi<sub>0.8</sub>Zr<sub>0.2</sub>O<sub>3</sub> samples were ascribed to the long-range ferroelectric order. However, by increasing Zr content in the sample BaTi<sub>0.8</sub>Zr<sub>0.2</sub>O<sub>3</sub>, a diffused ferroelectric peak was obtained resulting from the short-range ferroelectric order [40].

Table 4 illustrates that the saturation polarization ( $P_s$ ) and the remnant polarization ( $P_r$ ) values decrease and then increase as Zr content (x = 0.3). The increase in Zr content in B-sites perturbs the local structure due to the co-occupancy of Ti<sup>4+</sup> and Zr<sup>4+</sup> ions at the same crystallographic sites [41].

The value of the coercive field determines the ease with which the domains move. The lower  $E_c$  indicates that the domains move easily, which indicates that

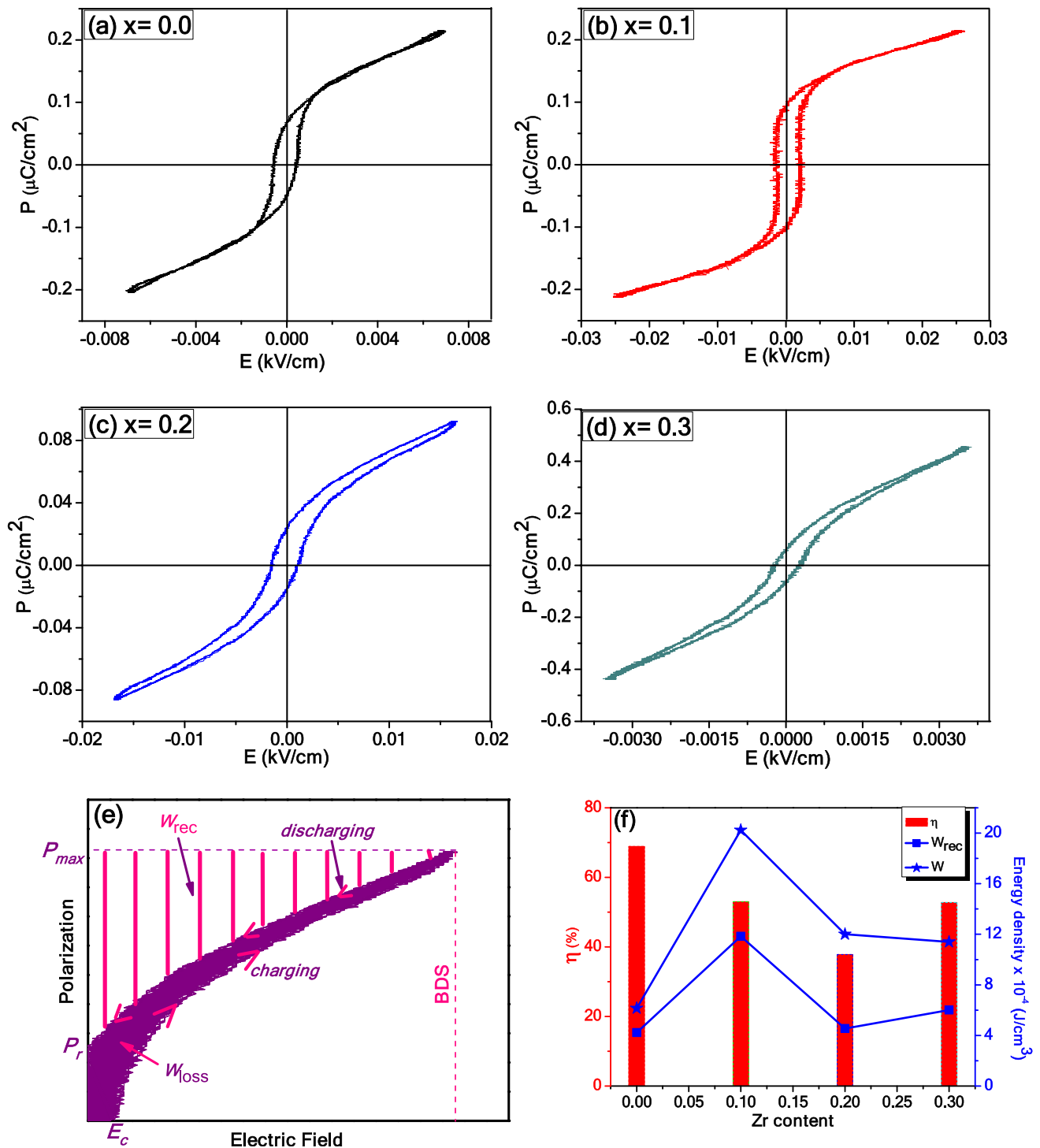


**Fig. 6** a–d P–E hysteresis loop for the investigated samples  $\text{BaTi}_{(1-x)}\text{Zr}_x\text{O}_3$ ; ( $x$ : 0.0, 0.1, 0.2, and 0.3) at room temperature. e The calculation of energy storage density and efficiency.

low energy loss during the sweep of the electric field enhances the ferroelectric properties [42]. The lowest  $E_c \sim 0.23 \times 10^{-4}$  kV/cm was obtained for ( $x = 0.3$ ) composition.

f Calculated energy density, recoverable energy storage density, and energy storage efficiency vs. Zr content

Table 4 shows the values of  $P_s$ ,  $P_r$ , and  $P_s - P_r$  as a function of Zr content. The  $P_s$  seems to be unchanged from ( $x = 0.0$ ) to ( $x = 0.1$ ) but it decreases significantly, for ( $x = 0.2$ ) then increases and reaches the

**Table 4** The values of saturation polarization ( $P_s$ ), remnant polarization ( $P_r$ ), coercive field ( $E_c$ ), the recoverable energy storage density ( $W_{rec}$ ), the energy loss density during discharge ( $W_{Loss}$ ), the total

energy storage density ( $W_t$ ), energy storage efficiency ( $\eta$ ), and the breakdown strength (BDS) of the samples  $BaTi_{1-x}Zr_xO_3$  ( $x = 0, 0.1, 0.2$  and  $0.3$ )

$BaTi_{1-x}Zr_xO_3$	$P_s$ ( $10^{-2}$ ) ( $\mu C/cm^2$ )	$P_r$ ( $10^{-2}$ ) ( $\mu C/cm^2$ )	$P_s-P_r$ ( $10^{-2}$ ) ( $\mu C/cm^2$ )	$E_c$ ( $10^{-4}$ ) (kV/cm)	Loop area ( $10^{-4}$ )(J/cm <sup>3</sup> )	$W_{rec}$ ( $10^{-4}$ ) (J/cm <sup>3</sup> )	$W_{loss}$ ( $10^{-4}$ ) (J/cm <sup>3</sup> )	$W_t$ ( $10^{-4}$ ) (J/cm <sup>3</sup> )	$\eta\%$	BDS (V/cm)
$x = 0.0$	21.5	5.7	15.8	5.08	7.45	4.23	1.91	6.15	68.89	6.99
$x = 0.1$	21.4	9.6	11.8	17.67	40.74	11.84	10.50	20.23	53.01	23.38
$x = 0.2$	9.2	1.9	7.3	12.59	16.49	4.54	7.46	12.00	37.81	16.46
$x = 0.3$	45.5	6.0	39.5	0.23	12.41	6.01	5.38	11.4	52.76	3.57

maximum value of  $45.5 \times 10^{-2} \mu C/cm^2$  at ( $x = 0.3$ ). This value increased by about 2.1 times than that of the parent sample value. A significant increase in  $P_r$  can be observed with the increased value of  $x$  and reaches the maximum value of  $9.6 \times 10^{-2} \mu C/cm^2$  for ( $x = 0.1$ ) then decreases to the lowest value of  $1.9 \times 10^{-2} \mu C/cm^2$  for  $x = 0.2$ . Thus, ( $P_s-P_r$ ) decreases with Zr content but it suddenly increases and reaches the maximum at ( $x = 0.3$ ) which is greater than the parent by 2.5 times so it may enhance the energy storage density [43]. Substitution of the large ionic radius cation  $Zr^{4+}$  instead of a smaller ionic radius cation  $Ti^{4+}$  could cause a decrease in the relative displacement of the large cation with respect to the oxygen octahedral cage [44]. We noticed that the largest value of the breakdown strength (BDS) was obtained for the sample at ( $x = 0.1$ ). This may be ascribed to the lowest grain size among the samples, where the smaller grain size enhances the breakdown strength. Although the sample at ( $x = 0.3$ ) has a lower grain size than the parent sample; however, the parent sample is slightly larger in BDS. This could be attributed to that the parent sample is finer than the ( $x = 0.3$ ) sample [45].

### 3.4.2 Energy storage analysis

Figure 6e represents a schematic diagram of the different parameters that affect the energy storage density and the efficiency of ferroelectric materials. The energy storage efficiency ( $\eta$ ) was computed from the following Eq. (8):

$$\eta = \frac{W_{rec}}{W_t} \tag{8}$$

where:  $W_{rec}$ : is the recoverable energy storage density,  $W_t$ : is the total energy storage density, which equals;

$$W_t = W_{rec} + W_{loss}$$

where:  $W_{Loss}$ : is the energy loss density during discharge.

The recoverable energy storage density  $W_{rec}$  could be obtained by integrating the area between the discharge curve and the maximum value of the polarization line ( $P_{max}$ ) of the P–E hysteresis loops according to the Eq. (9):

$$W_{rec} = \int_{P_r}^{P_{max}} EdP \tag{9}$$

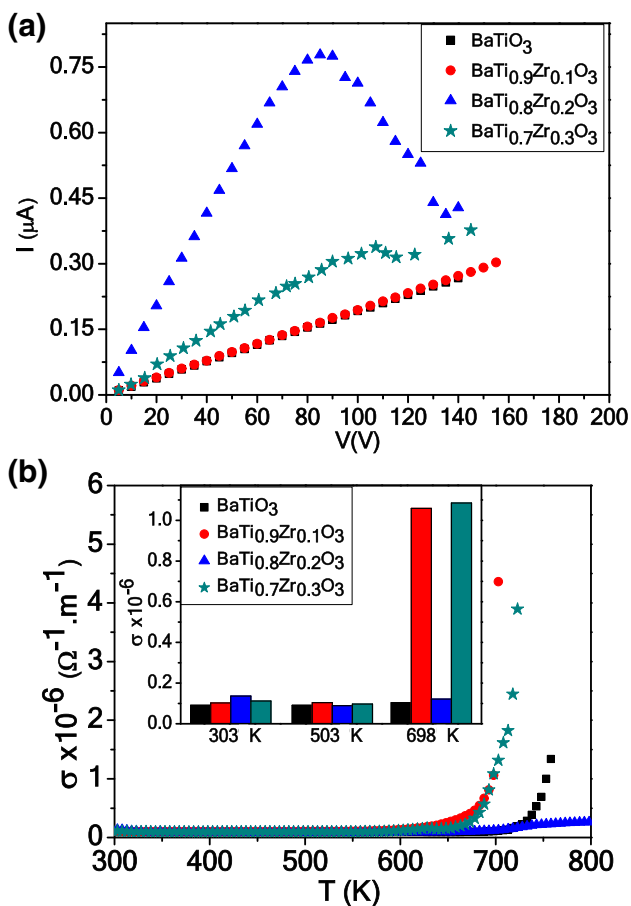
The energy loss density during discharge  $W_{Loss}$  could be obtained by integrating the area between charging and discharging curves of the P–E hysteresis loops [43, 45–47]. Figure 6e illustrates the domains of those integrations. We have used the OriginPro 8 software to integrate the selected areas.

Figure 6f shows the variation of  $W_{rec}$ ,  $W_t$  and  $\eta$  with Zr content and the values of those parameters in addition to  $W_{Loss}$  are calculated and listed in the Table 4. The maximum value of  $W_{rec}$  is observed at  $11.84 \times 10^{-4} J/cm^3$  for ( $x = 0.1$ ), which is greater than that observed for parent one  $4.23 \times 10^{-4} J/cm^3$  by 2.8 times. The enhancement in  $W_{rec}$  is attributed to the larger BDS [45]. For ( $x = 0.3$ ), the value of  $W_{rec}$  is greater than the parent by 1.42 times. The small increase in  $W_{rec}$  value is obtained for ( $x = 0.2$ ), it reaches  $4.54 \times 10^{-4} J/cm^3$  which is larger than the parent by only  $0.31 \times 10^{-4} J/cm^3$ . Although  $W_{rec}$  for the sample ( $x = 0.1$ ) is larger than that obtained for the sample ( $x = 0.3$ ) twice, the two samples have almost the same efficiency values (of about 53%) because of the largest energy loss density  $W_{loss}$  in ( $x = 0.1$ ). For the sample ( $x = 0.2$ ), it has a relatively large loss  $W_{loss}$  compared to the other samples, and it also has a relatively small  $W_{rec}$  and  $P_s-P_r = 7.3 \times 10^{-2}$

$\mu\text{C}/\text{cm}^2$ . Therefore, it has the lowest storage efficiency of 37.81%. For the parent sample,  $W_{\text{rec}}$  is not negligible as compared with both ( $x = 0.2$ ) and ( $x = 0.3$ ). It has the lowest  $W_f = 6.15 \times 10^{-4} \text{ J}/\text{cm}^3$  due to the lowest  $W_{\text{loss}} = 1.91 \times 10^{-4} \text{ J}/\text{cm}^3$ . Therefore, it has the largest efficiency of 68.89%. However, although the doping did not improve storage efficiency, it improved the recoverable density by a large percentage in the sample ( $x = 0.1$ ) compared to the parent and it increased slightly for ( $x = 0.2$ ) and ( $x = 0.3$ ).

### 3.5 DC electrical properties

Figure 7a depicts the I–V characteristic plot. The electric current intensity is found to be directly proportional to the potential difference for samples at ( $x = 0.0$  and 0.1). Non-ohmic behaviour above 85 V is very clear for ( $x = 0.2$  and 0.3). By increasing the

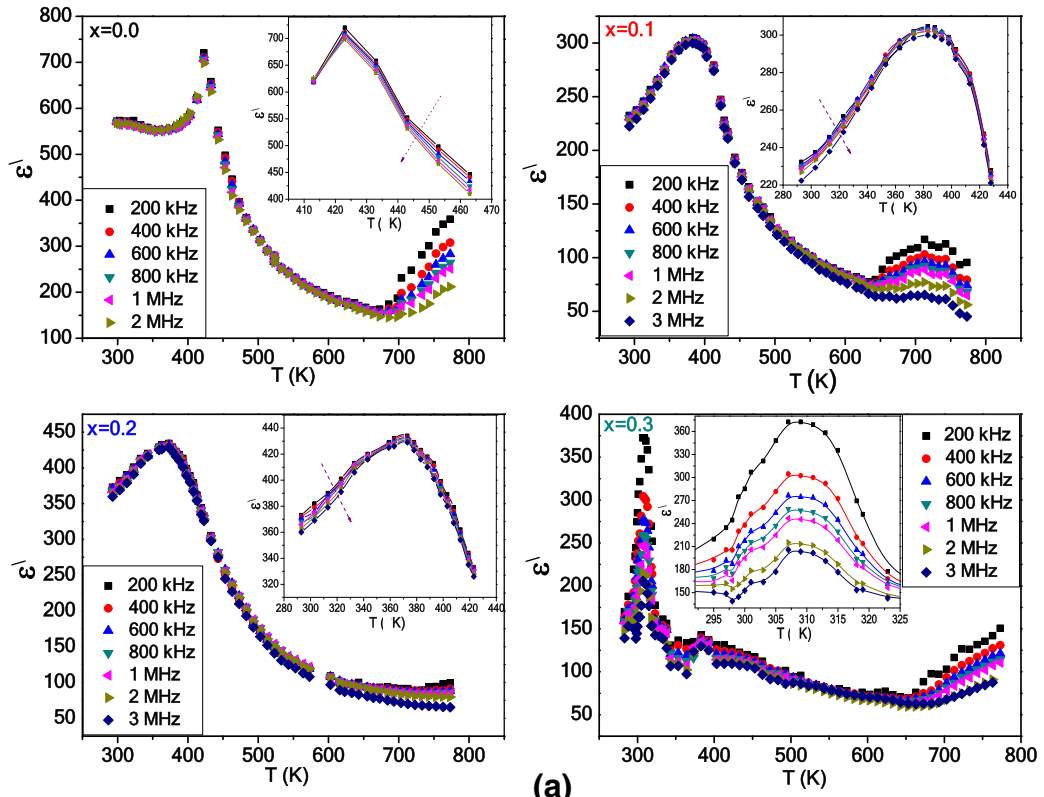


**Fig. 7** **a** I–V characteristic curve for the samples  $\text{BaTi}_{(1-x)}\text{Zr}_x\text{O}_3$ ; ( $x$ : 0.0, 0.1, 0.2, and 0.3). **b** The relation between dc conductivity and absolute temperature

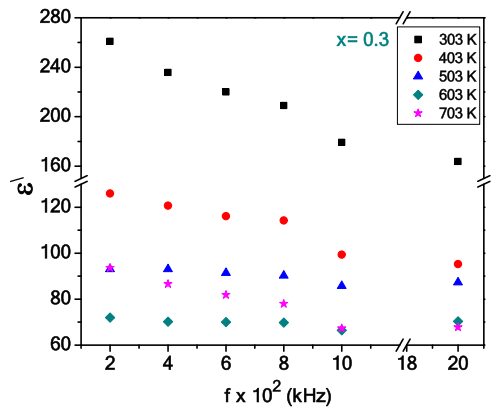
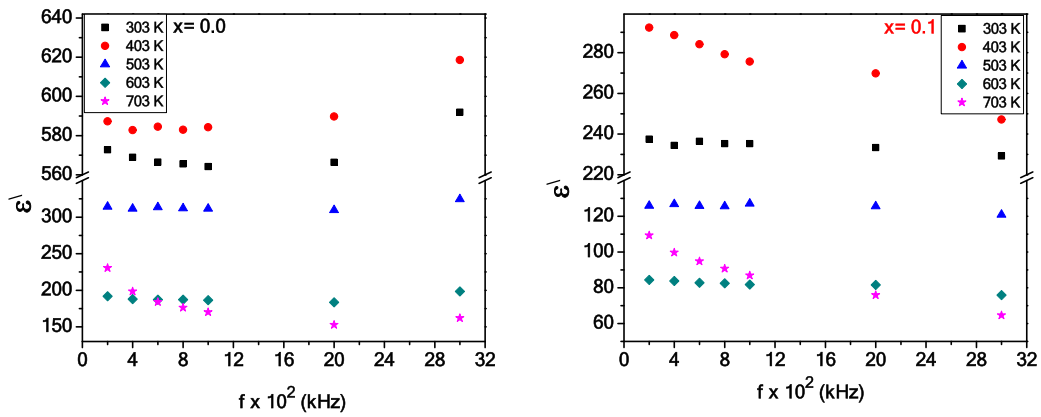
**Fig. 8** **a** Temperature dependence of dielectric permittivity for the investigated samples  $\text{BaTi}_{(1-x)}\text{Zr}_x\text{O}_3$ ; ( $x$ : 0.0, 0.1, 0.2, and 0.3) at different frequencies. **b** The frequency dependence of dielectric permittivity for the investigated samples  $\text{BaTi}_{(1-x)}\text{Zr}_x\text{O}_3$ ; ( $x$ : 0.0, 0.1, 0.2, and 0.3) at selected temperatures. **c** and **d** The variation of the maximum dielectric permittivity (Peak value of  $\epsilon'$ ) and its corresponding temperature (Peak position) with the frequency for the investigated samples respectively. **e** The dielectric constant ( $\epsilon'$ ) vs. the absolute temperature ( $T$ ) loops for ( $\text{BaTi}_{0.8}\text{Zr}_{0.2}\text{O}_3$ ) recorded at 200 kHz. **f** The variation of  $1/\epsilon'$  with the temperature for the investigated samples at 400 kHz. **g** The variation of  $\text{Ln}\left(\frac{1}{\epsilon'} - \frac{1}{\epsilon'_{\text{max}}}\right)$  as a function in  $\text{Ln}(T - T_{\text{max}})$  for the investigated samples at 400 kHz

zirconium content, the peak was observed and the non-ohmic conductivity shifted towards the higher voltages. For the sample  $\text{BaTi}_{0.8}\text{Zr}_{0.2}\text{O}_3$ , the values of electric current intensity have a peak at a potential difference of 85 V. It is clear that at Zr concentrations of 0.1 and 0.2, the current increases with increasing the applied voltage, whereas for high Zr content samples ( $x = 0.3$ ), the current decreases. This is due to the Zr ion being chemically more stable, which reduces the electron jump between  $\text{Ti}^{4+}$  and  $\text{Ti}^{3+}$ , thus increasing the resistivity of the  $\text{BaTi}_{0.7}\text{Zr}_{0.3}\text{O}_3$  sample [48, 49].

Figure 7a was used to perform the DC conductivity-temperature measurement at constant voltage. Figure 7b depicts the relationship between DC conductivity and absolute temperature in the samples  $\text{BaTi}_{1-x}\text{Zr}_x\text{O}_3$ . The DC conductivity values are nearly constant up to  $T = 650 \text{ K}$ , and then the DC conductivity increases due to the thermal energy that makes the molecules and ions more flexible to align under the effect of an electric field. The large thermal energy here increased the mobility of charge carriers, which consequently led to larger conductivity values. The inset Fig. 7b shows the variation of conductivity at selected temperatures with the Zr content. In-depth look at the electrical conductivity of the doped samples at room temperature 303 K, it appears to be slightly greater than the parent one, but the conductivity of the sample  $\text{BaTi}_{0.8}\text{Zr}_{0.2}\text{O}_3$ , increased about 1.5 times the parent. At a temperature 503 K higher than the room temperature, there is no noticeable difference in the electrical conductivity between the samples. But by looking at the conductivity behaviour at temperature 698 K, we noticed a significant increase in the electrical conductivity of the doped samples  $\text{BaTi}_{1-x}\text{Zr}_x\text{O}_3$  at ( $x = 0.1$  and 0.3), which reached about 10 times the parent sample. While the



(a)



(b)

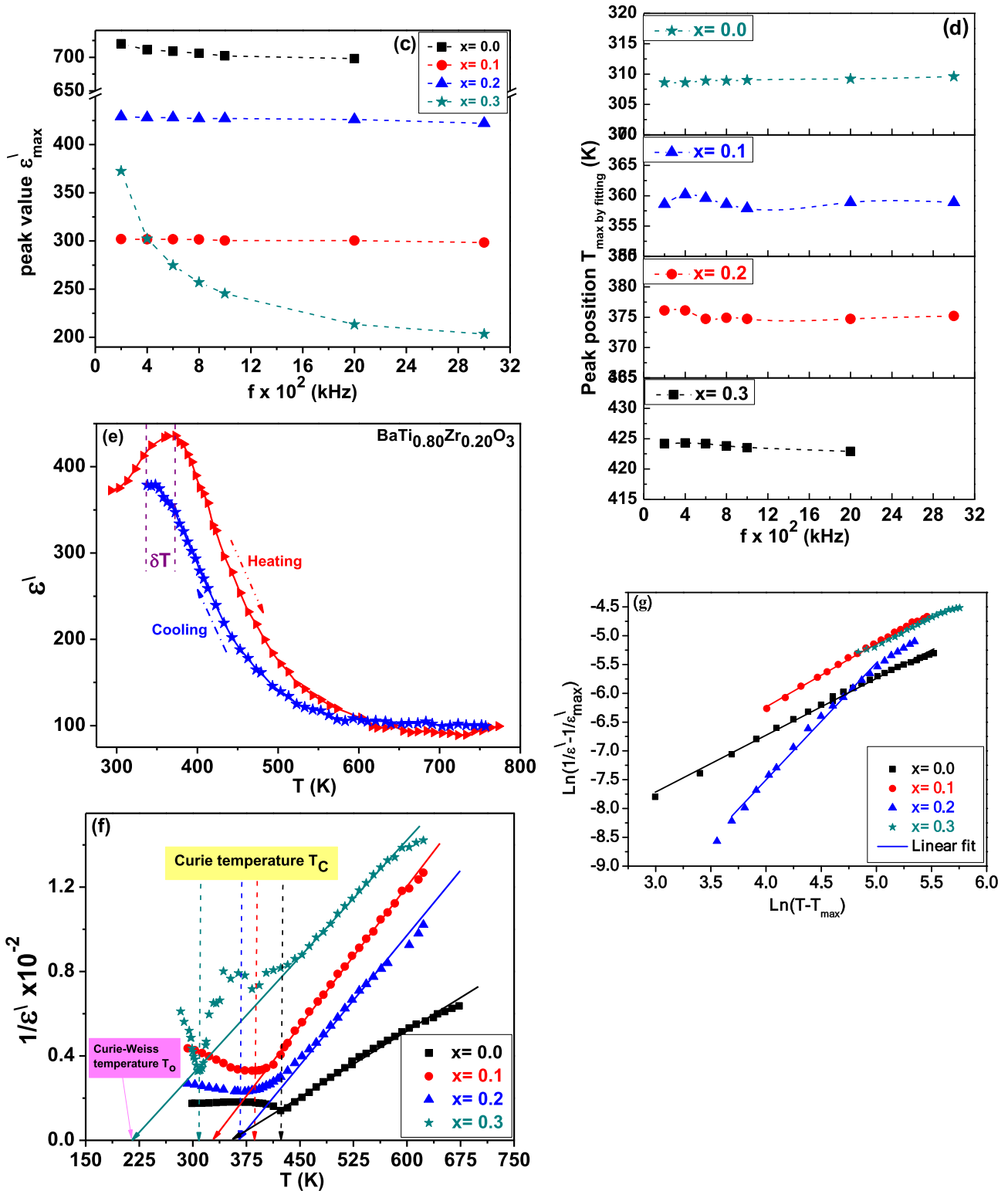


Fig. 8 continued

conductivity of the sample at ( $x = 0.2$ ) remained approximately constant and started with a very slight increase that appeared after a temperature of about 700 K, but its electrical conductivity is lower than that of the parent.

### 3.6 Dielectric characterization

Figure 8a compares the temperature dependence of dielectric permittivity for the  $\text{BaTi}_{1-x}\text{Zr}_x\text{O}_3$ ;  $x: 0.0, 0.1, 0.2,$  and  $0.3$  ceramic nanoparticles samples obtained at various frequencies. Looking at the figure, we notice the well-known peak of the ferroelectric materials from the ferroelectric to the paraelectric phase transition around a temperature known as the Curie temperature ( $T_C$ ). A slightly narrow peak is observed for the parent sample. By increasing Zr content, the broadening of the peak becomes larger for the doped samples at ( $x = 0.1$ ) and ( $x = 0.2$ ), respectively. By increasing Zr content, the broadening of the peak becomes larger for the doped samples at ( $x = 0.1$ ) and ( $x = 0.2$ ), respectively. A sharp peak is observed by a further increase in Zr content ( $x = 0.3$ ). To get a more accurate description of the peak transition, we fit the peak using a Gaussian fitting and estimate some parameters that help us

understand the nature and properties of this transition. Table 5 contains the values of the maximum dielectric constant (Peak value  $\epsilon'_{\max}$ ), the temperature corresponding to these values (Peak position  $T_{\text{maxbyfitting}}$ ) obtained by fitting the peak, and the full width at half maximum (FWHM).

The frequency dependence of dielectric permittivity for the investigated samples  $\text{BaTi}_{1-x}\text{Zr}_x\text{O}_3$ ; ( $x: 0.0, 0.1, 0.2,$  and  $0.3$ ) at selected temperatures is shown in Fig. 8b. The general trend is the decrease of the dielectric constant with increasing frequency. This is mainly interpreted as due to the lack of dipoles to the large external alternating frequency associated with the applied electric field.

Figure 8c shows the variation of the maximum dielectric constant with frequency. The dielectric change appears to be unnoticeable and decreases by a very small percentage with the increase in frequency for samples ( $x = 0.1$ ) and ( $x = 0.2$ ). By returning to the parent sample at ( $x = 0.0$ ), we observed a weak decrease in the dielectric constant  $\epsilon'_{\max}$  from 720 to 698 by increasing the frequency from 200 to 2000 kHz. At the sample ( $x = 0.3$ ), a strong decrease is observed. It decreases from 372.4 to 203.5 by 55% by increasing the frequency from 200 to 3000 kHz. This is interpreted as the weak response of the permanent

**Table 5** Peak transition estimated by fitting “The maximum dielectric constant (Peak value  $\epsilon'_{\max}$ ), the temperature corresponding to these values (Peak position  $T_{\text{maxbyfitting}}$ ), and the full width at half maximum (FWHM)

$\text{BaTi}_{1-x}\text{Zr}_x\text{O}_3$	Peak value $\epsilon'_{\max}$				Peak position $T_{\max}$				FWHM			
	$x = 0.0$	$x = 0.1$	$x = 0.2$	$x = 0.3$	$x = 0.0$	$x = 0.1$	$x = 0.2$	$x = 0.3$	$x = 0.0$	$x = 0.1$	$x = 0.2$	$x = 0.3$
200 kHz	720	301.9	429	372.4	424.2	376.1	358.6	308.6	18.5	76.8	77.0	18.7
400 kHz	711	301.8	428	302.3	424.3	376.1	360.2	308.6	18.0	76.9	75.2	17.7
600 kHz	709	301.7	428	274.7	424.2	374.7	359.6	308.9	18.1	79.6	82.5	16.8
800 kHz	706	301.5	427	257.0	423.8	374.9	358.6	308.9	18.5	78.6	87.0	16.0
1000 kHz	702	300.5	427	245.5	423.5	374.7	357.9	309.0	18.6	79.6	84.0	15.3
2000 kHz	698	300.4	426	213.3	422.9	374.7	358.9	309.2	18.9	79.8	85.0	13.2
3000 kHz	–	298.3	422	203.5	–	375.2	358.9	309.6	–	81.1	81.6	11.7
The average value of FWHM:-									18.4	78.9	81.8	16.3

**Table 6** The Values of The dielectric constant  $\epsilon'_o$  observed at room temperature ( $T_{\text{room}} = 303$  K), the Curie temperature ( $T_C$ ), The Curie–Weiss temperature ( $T_o$ ), the difference between  $T_C$  and  $T_o$  ( $\Delta T = T_C - T_o$ ), the Curie constant (C), and diffuseness exponent ( $\gamma$ ) were all measured at 400 kHz

	$\epsilon'_o$	$T_C$ (K)	$T_o$ (K)	$T_C - T_o$ (K)	$C \times 10^4$ (K)	$\gamma$
$\text{BaTiO}_3$	569	423	359	64	4.89	0.96
$\text{BaTi}_{0.9}\text{Zr}_{0.1}\text{O}_3$	234	386.5	329	57.5	2.31	1.10
$\text{BaTi}_{0.8}\text{Zr}_{0.2}\text{O}_3$	379	363	363	0	2.65	2.03
$\text{BaTi}_{0.7}\text{Zr}_{0.3}\text{O}_3$	261	308.5	218	90.5	3.00	0.91

dipoles by the increase of the frequency and the contribution of the charge carriers (ions) towards the dielectric constant decreasing [50]. Relaxation accompanies this decrease [51].

It's clear to see that the values of dielectric permittivity for the parent compound are higher compared to the Zr-doped samples. We set the values of the dielectric constant ( $\epsilon'_0$ ) at a room temperature of 303 K for all samples at 400 kHz. The results are listed in Table 6. The dielectric value of the parent sample is greater than what is observed by the doped sample since the dielectric constant of the parent sample is about 2.43 times the value observed at ( $x = 0.1$ ), 1.5 times the value observed at ( $x = 0.2$ ), and 2.18 times the value observed at ( $x = 0.3$ ).

According to Fig. 8a, the transition at 700 K may be due to Maxwell Wagner polarization, which was associated with grain boundary contribution, or to the presence of some oxygen vacancies in the annealed samples [52, 53]. The presence of a hump for BaTi<sub>0.9</sub>Zr<sub>0.1</sub>O<sub>3</sub> sample at about 700 K is due to the fact that the sample possesses the smallest grain size (= 130 nm) and leads to a migration of defect charges towards the grain boundaries [40].

The Curie temperature  $T_C$  of all samples is set from Fig. 8a at the maximum value of the dielectric constant at a frequency of 400 kHz and is included in Table 6. We can see that the Curie temperature  $T_C$  shifted towards lower temperatures by increasing the zirconium concentration. The reason behind that may be due to the larger ion radius of the Zr ion compared to the Ti ion [50, 54].

In the normal (non-relaxor) ferroelectric materials, the peak temperature  $T_{\max}$  does not depend on the measurement frequency, but in the relaxor ferroelectric materials, the dependence in frequency is noticeable [55]. Looking at Fig. 8d, which shows the variation of the peak position (peak position  $T_{\max\text{byfitting}}$ ) with the frequency, and back to the inset of Fig. 8a, which shows the dispersion of the dielectric curves at different frequencies around the peak phase transition, we observe that the position of the peak does not depend strongly on the frequency for ( $x = 0.0, 0.1, \text{ and } 0.3$ ), because the difference between its peak positions  $\Delta T_{\max}$  doesn't exceed 1.4 K for ( $x = 0.0$  and  $x = 0.1$ ) and 1 K for ( $x = 0.3$ ). So we cannot define whether the samples are normal or relaxor ferroelectric materials by indicating the variation of  $T_{\max}$  with frequency only. To make sure, we

shall evaluate a parameter called the diffuseness exponent ( $\gamma$ ) in a later section, which is a value that indicates exactly the type of the ferroelectric phase transition [56].

The FWHM of the dielectric constant is considered a good parameter to infer the degree of diffuseness of the phase transition. The larger the FWHM value, this indicates the presence of a high degree of diffuseness in the sample [55]. Table 5 illustrates the degree of diffusion in each sample at different values of frequency and its average values. We can see that the maximum diffusion is observed for the doped sample of ( $x = 0.2$ ), which is 4.45 times larger than the FWHM of the parent one. The doped sample of ( $x = 0.1$ ) shows approximately the same trend as at ( $x = 0.2$ ). It is 4.29 times larger than the FWHM of the parent one also. These values support the presence of high diffuse in transition at ( $x = 0.1$  and  $x = 0.2$ ). For the last doped one ( $x = 0.3$ ), the broadness of the peak is too small with an FWHM of only 16.3 K, which is close to the value obtained for the parent one. Thus, we could predict a very low degree of diffuseness.

Figure 8e shows the behaviour of the dielectric constant  $\epsilon'$  with the heating and cooling runs at the temperature of the sample BaTi<sub>0.8</sub>Zr<sub>0.2</sub>O<sub>3</sub>. After the transition of the FE-to-PE phase, the dielectric constant  $\epsilon'$  decreases with the increase in T. On cooling back, the material transforms from the paraelectric phase to the ferroelectric phase at a temperature that is slightly different from the temperature at which the transformation takes place while heating. We observed a clear thermal hysteresis, which supports the presence of the first-order phase transition. The transition temperature upon heating seems to be higher than that observed during cooling [57].

Figure 8f depicts the relationship between the reciprocal of the dielectric constant  $1/\epsilon'$  as a function of temperature ( $T$ ) at 400 kHz using Curie–Weiss law, Eq. (10) [58–60]:

$$\frac{1}{\epsilon'} = \frac{T}{C} - \frac{T_o}{C} \quad (10)$$

where ( $C$ ) is the Curie constant and ( $T_o$ ) is the Curie–Weiss temperature, were measured by fitting the linear paraelectric part of the plot. The extrapolated intersection of the plot with the temperature axis is the value of ( $T_o$ ) as shown, and we calculate the inverse of the slope of the linear fit to find ( $C$ ). A Curie constant with a magnitude of  $10^5$  K was



obtained for the displacement-type ferroelectrics, while a magnitude of  $10^3$  K was obtained for the order–disordered ferroelectrics [56]. For our investigated samples, we obtained a Curie constant with a magnitude of about  $10^4$  K. The porosity and the grain size affected the Curie constant [58]. The Curie constant decreases with the increase in the porosity and a decrease in the grain size. The parent sample has the highest Curie constant as it has the largest grain size, and Table 6 listed the values of  $C$ ,  $T_o$ ,  $T_C$ , and  $\Delta T$ : The difference between  $T_C$  and  $T_o$ .

The Curie temperature illustrates the equipose of the ferroelectric and paraelectric phases. At this temperature, the free energy of the ferroelectric phase is equal to that of the paraelectric phase. The stability of the ferroelectric phase is greater than that of the paraelectric phase for a temperature range between  $T_o$  and  $T_C$  while above  $T_C$  the paraelectric phase is more stable [60].

Table 6 illustrates that all samples have values of  $T_o$  smaller than  $T_C$  except for the doped sample of ( $x = 0.2$ ), where  $T_o$  is approximately equal to  $T_C$ .  $\Delta T$  decreases with the increase of Zr content but does not reach zero for the parent and doped samples of ( $x = 0.1$  and  $0.3$ ), which confirms that the ferroelectric transition of the first order [56, 59].

To identify whether our ferroelectric materials obey a first or second-order phase transition, we are going to calculate the diffuseness exponent ( $\gamma$ ) that describes the diffuse nature of the transition. The critical exponent for diffuse phase transformation ( $\gamma$ ) depends on the crystal structure, and thus the defects in the ceramic. It is in the range  $1 \leq \gamma \leq 2$ , where the value in between 1 and 2 corresponds to diffuse transition, when  $\gamma = 1$  to normal or non-relaxor ferroelectric materials, and values = 2 for the relaxor or completely diffuse ferroelectric materials [51, 58]. We have to fit the linear part of the modified Curie–Weiss law [58]:

$$\frac{1}{\epsilon'} - \frac{1}{\epsilon'_{\max}} = \frac{(T - T_C)^\gamma}{C'} \tag{11}$$

In the above expressions,  $\epsilon'$  is the dielectric constant,  $\epsilon'_{\max}$  is the maximum value of the dielectric constant,  $\gamma$  is the diffuseness exponent, and  $C'$  is the Curie–Weiss-like constant.

The plot of  $\ln\left(\frac{1}{\epsilon'} - \frac{1}{\epsilon'_{\max}}\right)$  as a function of  $\ln(T - T_{\max})$  is shown in Fig. 8g for all samples. The critical exponent  $\gamma$  is obtained from the slope of  $\ln\left(\frac{1}{\epsilon'} - \frac{1}{\epsilon'_{\max}}\right)$

versus  $\ln(T - T_{\max})$  plotted at 400 kHz for all samples and the values of  $\gamma$  listed in Table 6.

In our work, we achieved  $\gamma$  in the range nearest to the value of 1 for the parent and doped samples of ( $x = 0.1$  and  $0.3$ ) increasing in its value by increasing the width of the dielectric peak transition. These samples follow the first-order ferroelectric phase transition (non-relaxor ferroelectric materials). Where the sample of ( $x = 0.2$ )  $\gamma$  is equal to 2, therefore this sample exhibits a totally diffuse transition of a second-order ferroelectric (typical relaxor ferroelectric material) [51, 55, 56, 58].

Figure 9a represents the relation between conductivity, and the inset is  $\tan\delta$  as a function of the absolute temperature ( $T$ ). The results of the dielectric loss ( $\tan\delta$ ) seem to be in agreement with the results of the electrical conductivity ( $\sigma$ ) of all samples at the same frequency, where the electrical conductivity is related to the imaginary part of the dielectric constant [61].

$$\sigma(\omega) = \epsilon_o \omega \epsilon'' = \epsilon_o \omega \epsilon' \tan \delta \tag{12}$$

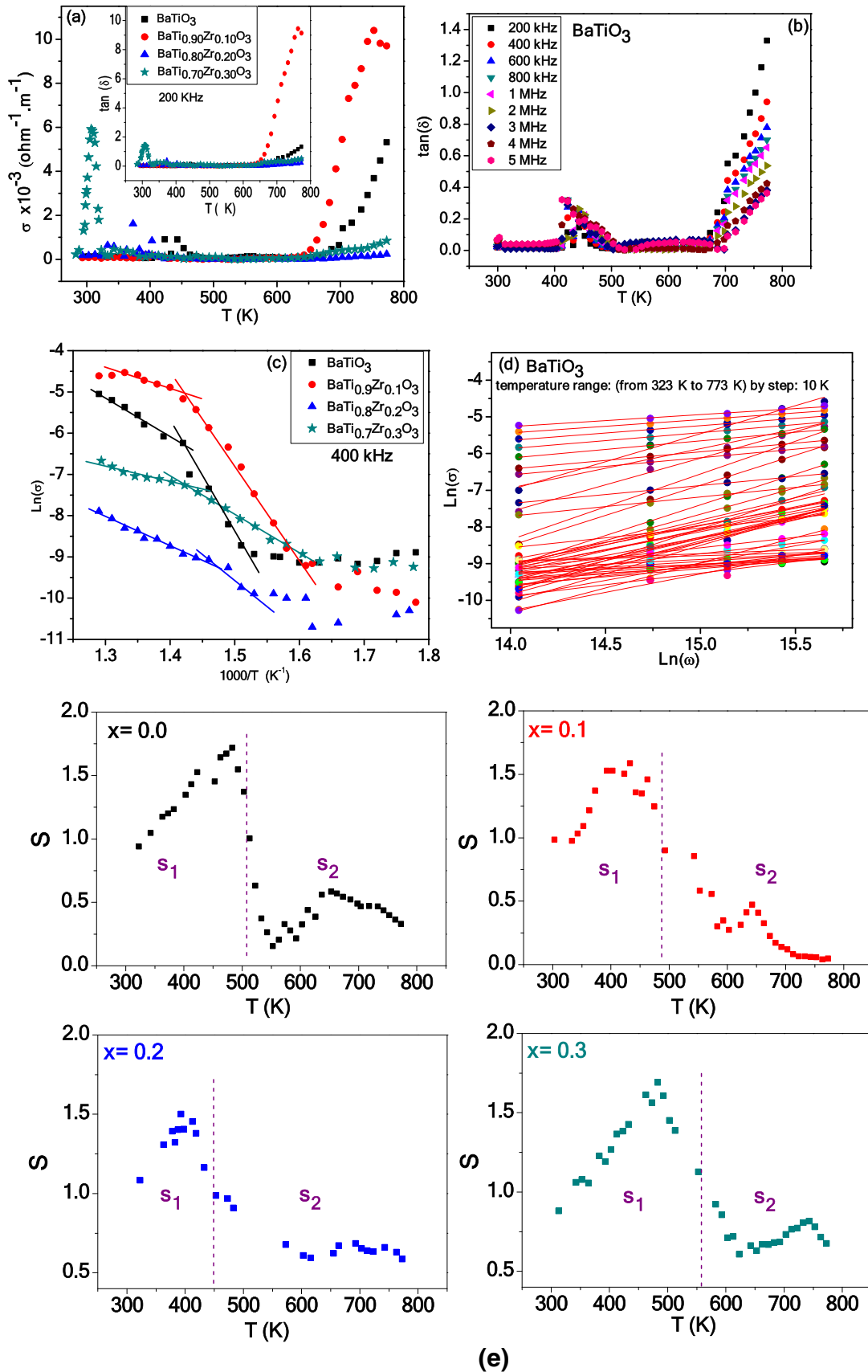
Figure 9b represents the dielectric loss ( $\tan\delta$ ) dependence on the absolute temperature at different frequencies for the parent sample. The domination of interface effects and space charge polarization at lower frequencies leads to a decrease in the value of  $\tan\delta$  as observed [58], we can also notice a peak around the transition at a temperature of about 423 K like which obtained for the dielectric constant (Fig. 8a).

Table 7 lists the electrical conductivity values at room temperature (303 K) at 800 kHz. We noticed that the electrical conductivity of the sample at ( $x = 0.3$ ) is about 10.4 times greater than that of the parent one ( $x = 0.0$ ), while it is almost equal to the parent sample at ( $x = 0.2$ ), and it is less than the parent by a value of about 0.4 times at ( $x = 0.1$ ).

Figure 9c illustrates the dependence of  $\ln \sigma$  ( $\sigma$ : conductivity) with the reciprocal of the absolute temperature ( $1000/T$ ) at 400 kHz for the investigated samples. The samples have a semiconducting like behaviour where the conductivity increases by increasing the temperature. The data obeys the well-known Arrhenius relation [61]:

$$\sigma = \sigma_o e^{\frac{-E}{kT}} \tag{13}$$

where  $E$  is the activation energy,  $k$  is the Boltzmann's constant, and  $T$  is the absolute temperature. The data of  $\ln \sigma$  ( $\sigma$ : conductivity) with the reciprocal of absolute temperature ( $1000/T$ ) has different slopes as



◀**Fig. 9** **a** The relation between the dielectric loss ( $\tan\delta$ ) and the absolute temperature ( $T$ ) at 200 kHz for the samples. **b** The dielectric loss ( $\tan\delta$ ) dependence on the absolute temperature at different frequencies for the parent sample. **c** The dependence of  $\ln \sigma$  on the reciprocal of the absolute temperature of all samples. **d** The relation between  $\ln \sigma$  and  $\ln \omega$  for the sample  $\text{BaTiO}_3$  as a function of the absolute temperature. **e** Dependence of the exponent  $S$  on the absolute temperature ( $T$ ) for the investigated samples  $\text{BaTi}_{(1-x)}\text{Zr}_x\text{O}_3$ ; ( $x$ : 0.0, 0.1, 0.2, and 0.3)

**Table 7** The activation energies  $E_I$  and  $E_{II}$  and the conductivity ( $\sigma$ ) of the investigated samples at 400 kHz

	$E_I$ (eV)	$E_{II}$ (eV)	$\sigma \times 10^{-4} \Omega^{-1} \text{m}^{-1}$ at 303 K
$\text{BaTiO}_3$	0.84	2.02	2.65
$\text{BaTi}_{0.9}\text{Zr}_{0.1}\text{O}_3$	0.47	1.94	1.45
$\text{BaTi}_{0.8}\text{Zr}_{0.2}\text{O}_3$	0.64	1.08	3.01
$\text{BaTi}_{0.7}\text{Zr}_{0.3}\text{O}_3$	0.36	0.78	56.04

shown in Fig. 9c which indicates the presence of different conduction mechanisms. The values of activation energies were calculated and reported in Table 7.

The thermal activation energy of the perovskite materials depends on many parameters, such as the grain (bulk), grain boundaries (the regions that separate one grain from another), and oxygen deficiency [62]. The activation energies for the grain are less than the grain boundary contributions. The values of grain size are calculated and reported in Table 1. The parent sample  $\text{BaTiO}_3$  has the greatest grain size (355 nm) and possesses large activation energies ( $E_I = 0.84$  eV,  $E_{II} = 2.02$  eV). The grain size values of Zr-doped samples are less than those of the parent  $\text{BaTiO}_3$ , and grain size values of Zr-doped samples are lower than those of the parent  $\text{BaTiO}_3$ , implying that the activation energies of Zr-doped samples are lower than those of the parent.

Figure 9d shows the relation between  $\ln \sigma$  on the  $y$ -axis and  $\ln \omega$  on the  $x$ -axis at different temperatures for the sample  $\text{BaTiO}_3$ . The data obeys the power law [63]:

$$\sigma_{AC}(\omega) = A\omega^s \tag{14}$$

where  $\sigma_{AC}$  is the ac conductivity,  $\omega = 2\pi f$  is the angular frequency,  $A$  is a temperature-dependent constant and  $s$  is the frequency-dependent exponent.

The values of the exponent  $s$  can be calculated from the slope of the straight line between  $\ln \sigma$  and  $\ln \omega$ . Figure 9e illustrates the dependence of  $s$  on absolute temperature ( $T$ ) for the investigated samples  $\text{BaTi}_{1-x}\text{Zr}_x\text{O}_3$ ;  $x = 0.0, 0.1, 0.2,$  and  $0.3$ . The values of  $s$  appear to be divided into two regions with changing temperatures, one in which  $1 < s_1 < 2$  and the other  $0 < s_2 < 1$ , where the dashed line in Fig. 9e separates these two regions. This plot determines the type of conduction mechanisms in the sample. The values of  $s$  increased with absolute temperature in the first temperature region, pointing to the small polaron (SP) hopping conduction mechanism [28, 63, 64], and for  $1 < s_1 < 2$  values it may be attributed to a well-localized hopping and/or reorientation motion [65, 66]. At high temperatures, correlated barrier hopping (CBH) is the main conduction mechanism. The  $\text{Zr}^{4+}$  ion is chemically more stable than the  $\text{Ti}^{4+}$  host cation. Therefore, the small polaron hopping mechanism is the main conduction mechanism in the first temperature region. The  $Zr/Ti$  ratio is a very important parameter for tailoring the ferroelectric-paraelectric phase transition.

### 3.7 Comparison with reported literatures

Table 8 compares our results with those reported earlier. We noticed that our samples are the largest in the transition temperature when compared with the results obtained by other authors [3, 67–71] in the parent sample and samples with  $x = 0.1$  and  $x = 0.2$ , therefore it may be useful in high-temperature applications.

When we compared our  $P_s$ ,  $P_r$ , and  $E_c$  with others, we find that our results are much lower than them for the  $x = 0.0$  and  $x = 0.1$  samples [3, 67–70]. This is due to the measurement at extremely low electric fields compared to the reported ones. We observe also a maximum dielectric constant at 200 kHz smaller than that obtained by Gaikwad at 100 kHz for the parent sample [67]. At  $x = 0.1$  we obtained a maximum dielectric constant at 200 kHz smaller than that obtained by Gaikwad at 100 kHz [67], I. ZOUARI at 100 kHz [69] and Sahanoor Islam [72], but for  $x = 0.3$  we obtained a maximum dielectric constant at  $x = 0.3$  greater than that obtained by Md Sahanoor Islam [72]. At room temperature (30 °C), our dielectric loss is smaller than that obtained by I. ZOUARI at (25 °C) for  $\text{BaTi}_{0.9}\text{Zr}_{0.1}\text{O}_3$  ceramic [69]. Overall, we have prepared the samples in an easier and faster way

**Table 8** Comparison between our work and the reported papers

Method of preparation	L (nm)	G S ( $\mu\text{m}$ )	$P_s$ ( $\mu\text{C}/\text{cm}^2$ )	$P_r$ ( $\mu\text{C}/\text{cm}^2$ )	$E_c$ (V/cm)	$T_c$ ( $^\circ\text{C}$ )	$\epsilon_r$ at $T_c$	$\epsilon_r$ at room temp	$\tan\delta$
0.0 Solid-state reaction method 1260 $^\circ\text{C}$ for 10 h [67]	–	–	10.44	1.59	930	126	5993.2		
Polymeric precursor route at 1300 $^\circ\text{C}$ for 2 h [68]	–	31				121			
Solid-state reaction 1200 $^\circ\text{C}$ for 6 h [3]		11.5		5.45	3140	120			
Polymeric precursor technique at 1300 $^\circ\text{C}$ for 2 h [70]		33		9.8	38,000	123			
sol–gel combustion at 1300 $^\circ\text{C}$ for 6 h [71]				1.45	151	123			
Our work	38.0	0.36	0.215	0.057	0.508	150	720.5 at 200 kHz	572.8 at 200 kHz	0.02
0.1 Solid-state reaction method 1260 $^\circ\text{C}$ for 10 h [67]	–	–	10.13	4.61	1550	100	2096.9		
solid-state reaction at 1250 $^\circ\text{C}$ for 12 h [69]	–	–	11.6		7900	88	7476	1832	0.08 at 25 $^\circ\text{C}$
Polymeric precursor technique at 1300 $^\circ\text{C}$ for 2 h [70]		12		6.8	26,000	82			
Sol–gel combustion at 1300 $^\circ\text{C}$ for 6 h [71]						94			
Solid-state reaction at 1200 $^\circ\text{C}$ for 4 h [72]	88.6	–					1444		
Our work	23.1	0.13	0.214	0.096	1.767	113.5	304	237.4	0.03
0.2 Polymeric precursor route at 1300 $^\circ\text{C}$ for 2 h [68]	–	0.7				37			
sol–gel combustion at 1300 $^\circ\text{C}$ for 6 h [71]	–	–				40			
Our work	19.3	0.15	0.092	0.019	1.259	90	435	375	0.04
0.3 Solid-state reaction at 1200 $^\circ\text{C}$ for 4 h [72]	31.0	–					238		
Our work	18.8	0.21	0.455	0.06	0.023	35.5	372.4	321.4	1.3

than other literature at lower annealing time and temperatures which reduces the cost. Our samples also exhibited a very low grain size and low crystallite size.

When comparing our results with those reported by Bappa Sona Kar, who prepared  $0.56\text{Bi}_{1-x}\text{La}_x\text{FeO}_3-0.44\text{BaTiO}_3$  ( $x = 0, 0.05, 0.10, 0.15,$  and  $0.20$ ) ceramics by using a conventional high-temperature solid-state reaction technique, calcined at  $840^\circ\text{C}$  for 5 h under an air atmosphere in a high-temperature furnace. The reported nanoparticles have relaxor ferroelectric properties with  $\gamma$  of 1.81, 1.85, 1.64, and 1.93 for 5%, 10%, 15%, and 20% La-doped BFO-BTO, respectively. In comparison to our results, the following values were obtained for  $\gamma$ : 0.96, 1.10, 2.03, and 0.91 for 0%,

10%, 20%, and 30% Zr-doped (BTZ). This directly means that we have non-relaxor ferroelectric properties for all samples except at ( $x = 0.2$ ). Our samples exhibit smaller average grain sizes (from 130 to 355 nm) when compared with pure, 10% and 20% La-doped BFO-BTO samples (from 200 to 600 nm). The average crystallite size for BFO-BTO ( $\approx 33$  nm) is not much smaller than our pure BTO one ( $= 38$  nm). We also found that the transition temperatures ( $T_c$ ) reported by Bappa Sona Kar are 583 K, 485 K, 471 K, and 407 K for the investigated nanoparticles of 5%, 10%, 15%, and 20% La-doped BFO-BTO. Whereas in our case, the transition temperatures ( $T_c$ ) are 423 K, 386.5 K, 363 K, and 308.5 K for 0%, 10%, 20%, and 30% Zr-doped (BTZ).

Bappa Sona Kar prepared a typical relaxor ferroelectric composite unlike our samples. Bappa Sona Kar samples consist of polar nanoregions and are characterized by a high saturation polarization, small remanent polarization, and coercive field [73].

## 4 Conclusion

The samples  $\text{BaTi}_{1-x}\text{Zr}_x\text{O}_3$  ( $x = 0.0, 0.1, 0.2,$  and  $0.3$ ) were prepared in a single-phase tetragonal structure. The lattice parameter of the samples increases with increasing Zr content. As shown from FESEM images, the average grain size of the samples is between 0.13 and 0.35  $\mu\text{m}$ . The P–E hysteresis loops ensure ferroelectric behaviour of the investigated samples due to the crystal's lack of a centre of symmetry. The ferroelectric properties were enhanced by Zr doping where  $E_c$  of the sample  $\text{BaTi}_{0.9}\text{Zr}_{0.1}\text{O}_3$  increased by 2 times compared with the parent sample. The sample  $\text{BaTi}_{0.9}\text{Zr}_{0.1}\text{O}_3$  characterized by a flattening of dielectric maximum which originates from the stress determined by grain size effects. We achieve  $\gamma$  in the range nearest to the value of 1 for the parent and doped samples of ( $x = 0.1$  and  $0.3$ ). These samples follow the first-order ferroelectric phase transition (non-relax or ferroelectric materials), whereas the sample of ( $x = 0.2$ )  $\gamma$  is equal to 2; therefore, this sample exhibits a totally diffuse transition of a second-order ferroelectric (typical relaxor ferroelectric material). This may be the reason behind the different behaviour of this sample compared to the other samples. The samples have a semiconducting like behaviour where the conductivity increases by increasing the temperature. The conduction mechanisms in the samples are small polaron (SP) hopping and correlated barrier hopping (CBH). The authors concluded that the samples can be used in many applications, such as heavy metal removal. The samples exhibited a larger transition temperature ( $T_c$ ) when compared with others, therefore, it may be useful in high-temperature applications. Our samples also exhibited very low grain sizes and low crystallite sizes.

## Author contributions

SIE-D put the idea of the paper. Mahasen Reda prepared the samples. MR, MMA, and SIE-D were

sharing: planning; Data curation; Formal analysis; methodology and experiments; discussing the results of the structure, microscopy, optical, and dielectric properties; writing draft and revising final form.

## Funding

Open access funding provided by The Science, Technology & Innovation Funding Authority (STDF) in cooperation with The Egyptian Knowledge Bank (EKB). No funding was received.

## Data availability

Data will be available upon request.

## Declarations

**Conflict of interest** The authors declare that they have no conflict of interest.

**Open Access** This article is licensed under a Creative Commons Attribution 4.0 International License, which permits use, sharing, adaptation, distribution and reproduction in any medium or format, as long as you give appropriate credit to the original author(s) and the source, provide a link to the Creative Commons licence, and indicate if changes were made. The images or other third party material in this article are included in the article's Creative Commons licence, unless indicated otherwise in a credit line to the material. If material is not included in the article's Creative Commons licence and your intended use is not permitted by statutory regulation or exceeds the permitted use, you will need to obtain permission directly from the copyright holder. To view a copy of this licence, visit <http://creativecommons.org/licenses/by/4.0/>.

## References

1. V. Reymond, S. Payan, D. Michau, J.P. Manaud, M. Maglione, Structural and electrical properties of  $\text{BaTi}_{1-x}\text{Zr}_x\text{O}_3$  sputtered thin films: effect of the sputtering conditions. *Thin Solid Films* **467**(1–2), 54–58 (2004). <https://doi.org/10.1016/j.tsf.2004.03.005>
2. B. Garbarz-Glos, A. Lisińska-Czekaj, D. Czekaj, W. Bak, Effect of semiconductor element substitution on the electric

- properties of barium titanate ceramics. *Arch. Metall. Mater.* **61**(2A), 887–890 (2016). <https://doi.org/10.1515/amm-2016-0150>
3. S. Mahajan, O.P. Thakur, C. Prakash, K. Sreenivas, Effect of Zr on dielectric, ferroelectric and impedance properties of BaTiO<sub>3</sub> ceramic. *Bull. Mater. Sci.* **34**(7), 1483–1489 (2011). <https://doi.org/10.1007/s12034-011-0347-2>
  4. A. Abdel Aal, T.R. Hammad, M. Zawrah, I.K. Battisha, A.B. Abou Hammad, FTIR study of nanostructure perovskite BaTiO<sub>3</sub> doped with both Fe<sup>3+</sup> and Ni<sup>2+</sup> ions prepared by sol-gel technique. *Acta Phys. Pol. A* **126**, 1318–1321 (2014). <https://doi.org/10.12693/APhysPolA.126.1318>
  5. A.G.A. Zubeda and B.I. Haider, Synthesis and characterization of nano sized pure and doped barium titanate powders prepared by sol-gel emulsion technique (2013).
  6. A. Kozyrev, V. Keis, V. Osadchy, A. Pavlov, O. Buslov, L. Sengupta, Microwave properties of (Ba, Sr)TiO<sub>3</sub> ceramic films and phase-shifters on their base. *Integr. Ferroelectr.* **34**(1–4), 189–195 (2001). <https://doi.org/10.1080/10584580108012888>
  7. J. Serraiocco et al., Tunable passive integrated circuits using BST thin films. *Integr. Ferroelectr.* **49**(2014), 161–170 (2002). <https://doi.org/10.1080/10584580215481>
  8. B. Liu, X. Wang, Q. Zhao, L. Li, Improved energy storage properties of fine-crystalline BaTiO<sub>3</sub> ceramics by coating powders with Al<sub>2</sub>O<sub>3</sub> and SiO<sub>2</sub>. *J. Am. Ceram. Soc.* **98**(8), 2641–2646 (2015). <https://doi.org/10.1111/jace.13614>
  9. S.H. Yoon, J.S. Park, C.H. Kim, D.Y. Kim, Difference between compositional and grain size effect on the dielectric nonlinearity of Mn and V-doped BaTiO<sub>3</sub> multilayer ceramic capacitors. *J. Appl. Phys.* **115**(24), 7 (2014). <https://doi.org/10.1063/1.4885155>
  10. Z. Yao et al., Homogeneous/inhomogeneous-structured dielectrics and their energy-storage performances. *Adv. Mater.* (2017). <https://doi.org/10.1002/adma.201601727>
  11. C. Laulhé, F. Hippert, R. Bellissent, A. Simon, G.J. Cuello, Local structure in BaTi<sub>1-x</sub>Zr<sub>x</sub>O<sub>3</sub> relaxors from neutron pair distribution function analysis. *Phys. Rev.* **79**, 1–10 (2009). <https://doi.org/10.1103/PhysRevB.79.064104>
  12. M. Paściak, M. Wołczyrz, A. Pietraszko, Interpretation of the diffuse scattering in Pb-based relaxor ferroelectrics in terms of three-dimensional nanodomains of the 110-directed relative interdomain atomic shifts. *Phys. Rev. B* **76**, 1–9 (2007). <https://doi.org/10.1103/PhysRevB.76.014117>
  13. R. LontioFomekong, S. You, R. Frohnhoven, T. Ludwig, S. Mathur, B. Saruhan, Self-decoration of barium titanate with rhodium-NP via a facile co-precipitation route for NO sensing in hot gas environment. *Sens. Actuators B* (2020). <https://doi.org/10.1016/j.snb.2021.129848>
  14. W. Li, Z. Xu, R. Chu, P. Fu, G. Zang, Dielectric and piezoelectric properties of Ba(Zr<sub>x</sub>Ti<sub>1-x</sub>)O<sub>3</sub> lead-free ceramics. *Braz. J. Phys.* **40**(3), 353–356 (2010). <https://doi.org/10.1590/S0103-97332010000300018>
  15. N. Wang, B.P. Zhang, J. Ma, L. Zhao, J. Pei, Phase structure and electrical properties of Sn and Zr modified BaTiO<sub>3</sub> lead-free ceramics. *Ceram. Int.* **43**(1), 641–649 (2017). <https://doi.org/10.1016/j.ceramint.2016.09.208>
  16. M.A. Ahmed, U. Seddik, N. Okasha, N.G. Imam, One-dimensional nanoferric rods; synthesis and characterization. *J. Mol. Struct.* **1099**, 330–339 (2015). <https://doi.org/10.1016/j.molstruc.2015.05.060>
  17. T.K. Kundu, A. Jana, P. Barik, Doped barium titanate nanoparticles. *Bull. Mater. Sci.* **31**(3), 501–505 (2008). <https://doi.org/10.1007/s12034-008-0078-1>
  18. S.K. Das, R.N. Mishra, B.K. Roul, Magnetic and ferroelectric properties of Ni doped BaTiO<sub>3</sub>. *Solid State Commun.* **191**, 19–24 (2014). <https://doi.org/10.1016/j.ssc.2014.04.001>
  19. P.D. Sc and M. Ali, Structural , Magnetic , and Transport Properties of Polymer-Nanoferrite Composites. (2013).
  20. P. Sateesh, J. Omprakash, G.S. Kumar, G. Prasad, Studies of phase transition and impedance behavior of Ba (Zr, Ti) O<sub>3</sub> ceramics. *J. Adv. Dielectr.* **5**, 1–13 (2015). <https://doi.org/10.1142/S2010135X15500022>
  21. C.D. Igwebike-Ossi, X-ray techniques. *Fail. Anal. Prev.* (2017). <https://doi.org/10.5772/intechopen.72447>
  22. M. Deluca et al., Investigation of the composition-dependent properties of BaTi<sub>1-x</sub>Zr<sub>x</sub>O<sub>3</sub> ceramics prepared by the modified Pechini method. *J. Eur. Ceram. Soc.* **32**(13), 3551–3566 (2012). <https://doi.org/10.1016/j.jeurceramsoc.2012.05.007>
  23. M.S. Mostari, M.J. Haque, S. Rahman Ankur, M.A. Matin, A. Habib, Effect of mono-dopants (Mg<sup>2+</sup>) and co-dopants (Mg<sup>2+</sup>, Zr<sup>4+</sup>) on the dielectric, ferroelectric and optical properties of BaTiO<sub>3</sub> ceramics. *Mater. Res. Express* (2020). <https://doi.org/10.1088/2053-1591/ab7e4c>
  24. R.D. Shannon, Revised effective ionic radii in halides and chalcogenides. *Acta Crystallogr. A* **32**, 751–767 (1976)
  25. P. Scherrer, Bestimmung der inneren Struktur und der Größe von Kolloidteilchen mittels Röntgenstrahlen. *Kolloidchem. Ein Lehrb.* **277**(1916), 387–409 (1912). [https://doi.org/10.1007/978-3-662-33915-2\\_7](https://doi.org/10.1007/978-3-662-33915-2_7)
  26. V. Uvarov, I. Popov, Metrological characterization of X-ray diffraction methods for determination of crystallite size in nano-scale materials. *Mater. Charact.* **58**(10), 883–891 (2007). <https://doi.org/10.1016/j.matchar.2006.09.002>
  27. X. Li, X. Lian, and F. Liu, Rear-end road crash characteristics analysis based on Chinese in-depth crash study data. In: *CICTP 2016 - Green Multimodal Transp. Logist. - Proc. 16th COTA Int. Conf. Transp. Prof.*, pp. 1536–1545 (2016). <https://doi.org/10.1061/9780784479896.140>

28. M.A. Ahmed, M.S. Selim, M.M. Arman, Novel multiferroic  $\text{La}_{0.95}\text{Sb}_{0.05}\text{FeO}_3$  orthoferrite. *Mater. Chem. Phys.* **129**(3), 705–712 (2011). <https://doi.org/10.1016/j.matchemphys.2011.03.033>
29. E.E. Ateia, B. Hussein, C. Singh, M.M. Arman, Multiferroic properties of  $\text{GdFe}_{0.9}\text{M}_{0.1}\text{O}_3$  ( $\text{M} = \text{Ag}^{1+}$ ,  $\text{Co}^{2+}$  and  $\text{Cr}^{3+}$ ) nanoparticles and evaluation of their antibacterial activity. *Eur. Phys. J. Plus* (2022). <https://doi.org/10.1140/epjp/s13360-022-02662-2>
30. W. Travis, E.N.K. Glover, H. Bronstein, D.O. Scanlon, R.G. Palgrave, On the application of the tolerance factor to inorganic and hybrid halide perovskites: a revised system. *Chem. Sci.* **7**(7), 4548–4556 (2016). <https://doi.org/10.1039/c5sc04845a>
31. Y. Chen et al., Ion doping effects on the lattice distortion and interlayer mismatch of aurivillius-type bismuth titanate compounds. *Materials* (Basel) (2018). <https://doi.org/10.3390/ma11050821>
32. E.E. Ateia, M.M. Arman, E. Badawy, Role of coupling divalent cations on the physical properties of  $\text{SmFeO}_3$  prepared by citrate auto-combustion technique. *Appl. Phys. A* **125**(8), 1–7 (2019). <https://doi.org/10.1007/s00339-019-2795-2>
33. M.M. Arman, S.I. El-Dek, Role of annealing temperature in tailoring Ce-doped  $\text{LaFeO}_3$  features. *J. Phys. Chem. Solids* (2021). <https://doi.org/10.1016/j.jpcs.2021.109980>
34. M. Zhu, L. Liu, Y. Hou, H. Wang, H. Yan, Microstructure and electrical properties of MnO-doped  $(\text{Na}_{0.5}\text{Bi}_{0.5})_{0.92}\text{Ba}_{0.08}\text{TiO}_3$  lead-free piezoceramics. *J. Am. Ceram. Soc.* **90**(1), 120–124 (2007). <https://doi.org/10.1111/j.1551-2916.2006.01349.x>
35. A. Kheyrdan, H. Abdizadeh, A. Shakeri, M.R. Golobostanfard, Structural, electrical, and optical properties of sol-gel-derived zirconium-doped barium titanate thin films on transparent conductive substrates. *J. Sol-Gel Sci. Technol.* **86**(1), 141–150 (2018). <https://doi.org/10.1007/s10971-018-4610-5>
36. A. Ansón-Casaos, I. Tacchini, A. Unzue, M.T. Martínez, Combined modification of a  $\text{TiO}_2$  photocatalyst with two different carbon forms. *Appl. Surf. Sci.* **270**, 675–684 (2013). <https://doi.org/10.1016/j.apsusc.2013.01.120>
37. T.A. Khalyavka, N.D. Shcherban, V.V. Shymanovska, E.V. Manuilov, V.V. Permyakov, S.N. Shcherbakov, Cerium-doped mesoporous  $\text{BaTiO}_3/\text{TiO}_2$  nanocomposites: structural, optical and photocatalytic properties. *Res. Chem. Intermed.* **45**(8), 4029–4042 (2019). <https://doi.org/10.1007/s11164-019-03888-z>
38. H. Wang et al., Preparation of  $\text{BaTiO}_3@/\text{NiO}$  core-shell nanoparticles with antiferroelectric-like characteristic and high energy storage capability. *J. Eur. Ceram. Soc.* **41**(7), 4129–4137 (2021). <https://doi.org/10.1016/j.jeurceramsoc.2021.02.042>
39. M.A. Ahmed, N. Okasha, N.G. Imam, Advanced imaging techniques for characterization of  $0.5\text{BaTiO}_3/0.5\text{Ni}_0.5\text{Zn}_0.5\text{Fe}_2\text{O}_4$  multiferroic nanocomposite. *J. Alloys Compd.* **557**, 130–141 (2013). <https://doi.org/10.1016/j.jallcom.2012.12.036>
40. M. Habib et al., Piezoelectric performance of Zr-modified lead-free  $\text{BiFeO}_3\text{--BaTiO}_3$  ceramics. *Mater. Res. Bull.* **146**(March), 2022 (2021). <https://doi.org/10.1016/j.materresbull.2021.111571>
41. A. Kumar et al., Atomic-resolution electron microscopy of nanoscale local structure in lead-based relaxor ferroelectrics. *Nat. Mater.* **20**(1), 62–67 (2021). <https://doi.org/10.1038/s41563-020-0794-5>
42. M.A.L. Grace, R. Sambasivam, R.N. Perumal, V. Athikesavan, Enhanced synthesis, structure, and ferroelectric properties of Nb-modified  $1-x [\text{Bi}_{0.5}(\text{Na}_{0.4}\text{K}_{0.1}) (\text{Ti}_{1-x}\text{Nb}_x)] \text{O}_{3-x}(\text{Ba}_{0.7}\text{Sr}_{0.3})\text{TiO}_3$  ceramics for energy storage applications. *J. Aust. Ceram. Soc.* **56**(1), 157–165 (2020). <https://doi.org/10.1007/s41779-019-00441-4>
43. H. Yang, F. Yan, Y. Lin, T. Wang, Enhanced recoverable energy storage density and high efficiency of  $\text{SrTiO}_3$ -based lead-free ceramics. *Appl. Phys. Lett.* (2017). <https://doi.org/10.1063/1.5000980>
44. Z. Cen et al., Effect of  $\text{Zr}^{4+}$  substitution on thermal stability and electrical properties of high temperature  $\text{BiFe}_{0.99}\text{Al}_{0.01}\text{O}_3\text{--BaTi}_{1-x}\text{Zr}_x\text{O}_3$  ceramics. *J. Alloys Compd.* **567**, 110–114 (2013). <https://doi.org/10.1016/j.jallcom.2013.03.065>
45. W. Ma et al., Enhanced energy-storage performance with excellent stability under low electric fields in BNT-ST relaxor ferroelectric ceramics. *J. Mater. Chem. C* **7**(2), 281–288 (2019). <https://doi.org/10.1039/c8tc04447c>
46. Z. Ma et al., Modeling of hysteresis loop and its applications in ferroelectric materials. *Ceram. Int.* **44**(4), 4338–4343 (2018). <https://doi.org/10.1016/j.ceramint.2017.12.027>
47. V. Veerapandiyam, F. Benes, T. Gindel, M. Deluca, Strategies to improve the energy storage properties of perovskite lead-free relaxor ferroelectrics: a review. *Materials* (Basel) **13**(24), 1–47 (2020). <https://doi.org/10.3390/ma13245742>
48. M.N.V. Ramesh, K.V. Ramesh, Structural, dielectric and AC conductivity studies on  $0.8\text{Ba}_{0.2}(\text{Bi}_{0.5}\text{K}_{0.5})\text{Ti}_{1-x}\text{Zr}_x\text{O}_3$  lead free ceramic system. *Mater. Sci. Pol.* **34**(3), 669–675 (2016). <https://doi.org/10.1515/msp-2016-0088>
49. N. Gouitaa, L. Taj-Dine, A. Farid, A.F. Zahra, Structural, dielectric and electrical properties of modified  $\text{BaTi}_{0.80}\text{Fe}_{0.20}\text{O}_3$  ceramics by Zr addition in ti site at  $x = 0.00$  to  $0.10$ . *Iran. J. Mater. Sci. Eng.* **18**(3), 1–12 (2021). <https://doi.org/10.22068/ijmse.2059>
50. U. Ahmadu, A. Muazu, S. Umar, Physical properties of porous pure and Zr/Sn-doped nanocrystalline  $\text{BaTiO}_3$

- ceramics. Recent Adv. Porous Ceram. (2018). <https://doi.org/10.5772/intechopen.75500>
51. A. El Ghandouri, S. Sayouri, T. Lamcharfi, L. Hajji, Effect of strontium on the structural and piezoelectric properties of the sol–gel processed barium titanate. *J. Ceram. Process. Res.* **19**(2), 154–170 (2018)
  52. I. Rivera, A. Kumar, N. Ortega, R.S. Katiyar, S. Lushnikov, Divide line between relaxor, diffused ferroelectric, ferroelectric and dielectric. *Solid State Commun.* **149**(3–4), 172–176 (2009). <https://doi.org/10.1016/j.ssc.2008.10.026>
  53. C.E. Ciomaga, M.T. Buscaglia, V. Buscaglia, L. Mitoseriu, Oxygen deficiency and grain boundary-related giant relaxation in Ba(Zr, Ti)O<sub>3</sub> ceramics. *J. Appl. Phys.* (2011). <https://doi.org/10.1063/1.3664749>
  54. C. Composites, Electrophysical properties of PMN-PT-ferrite (2019).
  55. A. Niemer, R. Pankrath, K. Betzler, M. Burianek, M. Muehlberg, Dielectric properties and the phase transition of pure and cerium doped calcium–barium–niobate. *World J. Condens. Matter Phys.* **02**(02), 80–84 (2012). <https://doi.org/10.4236/wjcmp.2012.22014>
  56. X.L. Zhu, X.M. Chen, Ferroelectric transition and Curie–Weiss behavior in some filled tungsten bronze ceramics. *Chin. Phys. Lett.* **31**(1), 1–5 (2014). <https://doi.org/10.1088/0256-307X/31/1/015201>
  57. S. Chaudhary, A.K. Sisodia, D.C. Dube, Thermal hysteresis across the first-order phase transition in the (Na<sub>0.5</sub>Bi<sub>0.5</sub>)<sub>1-x</sub>Ba<sub>x</sub>TiO<sub>3</sub> dielectric system. *Phase Trans.* **78**(12), 895–904 (2005). <https://doi.org/10.1080/01411590500404901>
  58. T. Ohji, M. Singh, and S. Mathur, Tatsuki Ohji, Mrityunjay Singh and Sanjay Mathur Copyright © 2015 The American Ceramic Society. **3**, 197–203, (2015)
  59. A.A. Bahgat, B.A.A. Makram, E.E. Shaisha, M.M. El-Desoky, Ferroelectricity in the glassy material of the composition Bi<sub>2</sub>O<sub>3</sub>–Pb<sub>3</sub>O<sub>4</sub>–CuO–K<sub>2</sub>O. *J. Alloys Compd.* **506**(1), 141–150 (2010). <https://doi.org/10.1016/j.jallcom.2010.06.161>
  60. C. Wang, Theories and methods of first order ferroelectric phase transitions. *Ferroelectrics* (2010). <https://doi.org/10.5772/13359>
  61. M.M. Arman, S.I. El-Dek, Enhancement in dielectric and optical properties of La<sub>1-x</sub>Ce<sub>x</sub>FeO<sub>3</sub> nanoparticles. *J. Mater. Res. Technol.* **8**(6), 5396–5404 (2019). <https://doi.org/10.1016/j.jmrt.2019.09.006>
  62. B. Garbarz-Glos, W. Bąk, A. Budziak, P. Dulian, A. Lisińska-Czekaj, D. Czekaj, The application of the mechanochemical synthesis for the preparation of advanced ceramics based on barium titanate. *Arch. Metall. Mater.* **65**(4), 1391–1396 (2020). <https://doi.org/10.24425/amm.2020.133705>
  63. S.R. Elliott, A.C. conduction in amorphous chalcogenide and pnictide semiconductors. *Adv. Phys.* **36**(2), 135–217 (1987). <https://doi.org/10.1080/00018738700101971>
  64. K. Kumari, A. Prasad, K. Prasad, Dielectric, impedance/modulus and conductivity studies lead-free ceramics. *Am. J. Mater. Sci.* **6**(1), 1–18 (2016). <https://doi.org/10.5923/j.materials.20160601.01>
  65. K.J. Hamam et al., Temperature and frequency effect on the electrical properties of bulk nickel phthalocyanine octacarboxylic acid (Ni-Pc(COOH)<sub>8</sub>). *Appl. Phys. A* (2019). <https://doi.org/10.1007/s00339-018-2147-7>
  66. M.F. Mostafa, A.A.A. Youssef, S.S. El-Hakim, Magnetic and electric studies of a new Co(II) perovskite-like material. *Phase Trans.* **77**(3), 317–333 (2004). <https://doi.org/10.1080/01411590310001639222>
  67. S.K. Gaikwad et al., Effect of Zr<sup>4+</sup> substitution on ferroelectric and dielectric properties of BaTiO<sub>3</sub> ceramics. *AIP Conf. Proc.* **1731**(2016), 4–7 (2016). <https://doi.org/10.1063/1.4948227>
  68. T.M. Amaral, E. Antonelli, D.A. Ochoa, J.E. García, A.C. Hernandez, Microstructure effects on BaTiO<sub>3</sub>/BaTi<sub>0.8</sub>Zr<sub>0.2</sub>O<sub>3</sub> composites properties. *Ceram. Int.* **42**(7), 8488–8494 (2016). <https://doi.org/10.1016/j.ceramint.2016.02.071>
  69. I. Zouari et al., Effects of Er<sup>3+</sup> and Pr<sup>3+</sup> substitution on structural, dielectric, ferroelectric and photoluminescence properties of the BaTi<sub>0.9</sub>Zr<sub>0.1</sub>O<sub>3</sub> ceramic. *J. Electron. Mater.* **46**(7), 4662–4669 (2017). <https://doi.org/10.1007/s11664-017-5451-7>
  70. T.M. Amaral, E. Antonelli, D.A. Ochoa, J.E. García, A.C. Hernandez, Microstructural features and functional properties of bilayered BaTiO<sub>3</sub>/BaTi<sub>1-x</sub>Zr<sub>x</sub>O<sub>3</sub> ceramics. *J. Am. Ceram. Soc.* **98**(4), 1169–1174 (2015). <https://doi.org/10.1111/jace.13417>
  71. M. Aghayan, A. Khorsand Zak, M. Behdani, A. Manaf Hashim, Sol–gel combustion synthesis of Zr-doped BaTiO<sub>3</sub> nanopowders and ceramics: dielectric and ferroelectric studies. *Ceram. Int.* **40**, 16141–16146 (2014). <https://doi.org/10.1016/j.ceramint.2014.07.045>
  72. M.S. Islam, J. Ghosh, Study of non-centrosymmetric to centrosymmetric structural transformation in Zr-doped barium titanate. *Phase Trans.* **93**(4), 351–360 (2020). <https://doi.org/10.1080/01411594.2020.1731509>
  73. B.S. Kar, M.N. Goswami, P.C. Jana, Effects of lanthanum dopants on dielectric and multiferroic properties of BiFeO<sub>3</sub>–BaTiO<sub>3</sub> ceramics. *J. Alloys Compd.* **861**, 157960 (2021). <https://doi.org/10.1016/j.jallcom.2020.157960>

**Publisher's Note** Springer Nature remains neutral with regard to jurisdictional claims in published maps and institutional affiliations.